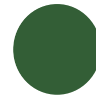

Determination of stress in Ti-NiV supermirrors

Marius Folden Simonsen
Ursula Bengaard Hansen

Bachelor Project in Physics

Niels Bohr Institutet
University of Copenhagen
August 29, 2011

Supervisors: Thierry Bigault and Kim Lefmann

Resumé

Multilagssuperspejle til at lede neutroner fra neutronkilder til forsøgsopstillinger ved neutronforskningscentre som *ILL* [1] og det fremtidige *ESS* [2] er næsten uundværlige. Superspejle består af flere hundrede eller tusinde lag, og de mange lag skaber en tilsvarende høj mekanisk spænding i spejlet, der i sidste ende kan få spejlet til at løsne sig fra det underlag, det normalt sidder på. Dette er en af de største begrænsninger inden for konstruktionen af superspejle.

Spændingen i et spejl får underlaget til at bøje, og krumningen af underlaget kan bruges sammen med Stoney-ligningen til at udregne størrelsen af spændingen. Den første del af dette projekt handlede om at undersøge den daværende metode til at udregne krumningen af underlaget og at udvikle en ny og mere præcis metode. Vi har udført vores målinger med et Twyman-Green-interferometer i the Mirror and Metrology Laboratory [3] på the European Synchrotron Radiation Source, *ESRF* [4]. Med den nye metode til krumningsbestemmelse er usikkerheden på den reciprokke krumningsradius under $20 \cdot 10^{-6}\text{m}^{-1}$, hvilket er fem gange bedre end med den gamle metode.

Den anden del af projektet gik ud på at bestemme parametrene i en model for spændingen i et superspejl. Seks periodiske Titanium-NikkelVanadium multilag og et superspejl blev fremstillet ved hjælp af metoden magnetron sputtering, og spændingen i hvert multilag blev målt. Ved hjælp af resultaterne fra disse målinger kunne vi estimere størrelsen af parametrene. Med disse parameterværdier forudsagde vores model en spænding i et bestemt superspejl på -535 ± 33 MPa, mens den målte værdi var -579 ± 7 MPa. Det giver en forskel på kun 8%, hvilket er acceptabelt i forhold til måleusikkerhederne.

Abstract

Today supermirrors to guide neutrons from neutron sources to instruments at neutron research facilities like *ILL* [1] and the future *ESS* [2] are nearly indispensable. Supermirrors are made out of several hundreds or even thousands of individual layers of metallic film, and the large number of layers leads to a corresponding large amount of stress in the mirrors. This may result in the mirrors peeling off and is today one of the biggest limitations in supermirror construction [5].

The stress is calculated using the Stoney equation [6], after having measured the curvature of the substrate induced by the film stress. The first part of this project focuses on an evaluation of the existing method for substrate curvature measurement and the developement of a new and more precise method. We have performed our curvature measurements with a Twyman-Green interferometer in the Mirrror and Metrology Laboratory [3] at the European Synchrotron Radiation Facility, *ESRF* [4]. With our new method, the error on the the reciprocal curvature radius is below $20 \cdot 10^{-6}\text{m}^{-1}$, which is a 5 time improvement over the old method.

The second part of our project focuses on a model for stress determination in supermirrors [7]. Six Ti NiV periodic multilayers and one supermirror were produced using magnetron sputtering, and the stress in each multilayer was measured. The results led us to a preliminary determination of the parameters in the model. With our parameters the model predicted the stress in our supermirror to be -535 ± 33 MPa which only differ from the measured stress -579 ± 7 MPa by 8% and is consistent with the error bars.

Preface and acknowledgements

Working in the Multilayer Laboratory at the Institut Laue-Langevin [1] has been a great experience for us. It has introduced us to how research is made at the worlds leading neutron research facility [1]. We would therefore like to thank Pierre Courtois for hosting us in the Neutron Optics Service Group. We also thank Ken Andersen from ESS [2] for arranging the contact.

In the Multilayer Laboratory the development and production of supermirrors for *ILL* takes place. We would like to thank our supervisor Thierry Bigault, the responsible of the Multilayer Laboratory, for his guidance and numerous explanations. We would as well like to show our gratitude to Guillaume Delphin and Vincent Gaignon for the time and work they have put into the production of the samples we have used in this project.

We would also like to thank Raymond Barrett and Amparo Vivo for letting us take our measurements in the Mirror and Metrology Laboratory at the European Synchrotron Radiation Facility, *ESRF* [4], and for the help we received there. Our thanks also go to Christian Morawe, the responsible for the Multilayer Laboratory at *ESRF*, for explaining the work he has performed on stress in multilayer structures.

A special thank goes to Sonja Lindahl Holm for her encouragement and help during the final days of the project. Finally we would like to thank our supervisor Kim Lefmann for his guidance and advice.

Contents

Abstract i

Preface and acknowledgements ii

1 Motivation 1

2 Introduction 1

3 Thermal neutron scattering 2
3.1 Neutron scattering cross section 2
3.2 Fermi pseudo potential 4
3.3 Coherent scattering and neutron optics 5
3.4 Index of refraction 6

4 Reflection 6
4.1 Critical angle 6
4.2 Reflection from a multilayer 7

5 Thin film stress 8
5.1 Aspects of elasticity theory 9
5.2 Determining thin film stress by substrate curvature measurement 10
5.3 The Stoney equation for the silicon (111) wafer 11

6 Experimental setup 12
6.1 Choice of substrate 12
6.2 Thin film deposition by magnetron sputtering 13
6.3 The *FISBA* Twyman-Green interferometer 14

7 A new method for calculating the effective curvature radius 15
7.1 The 1/R Method 15
7.2 The 12th Order Method 16
7.3 Improved precision with the 12th Order Method 16
7.3.1 Different lengths 17
7.3.2 Perpendicular displacement 17
7.3.3 Changing the *FISBA* support 18
7.3.4 Repeatability 19
7.3.5 Moving the sample between measurements 19
7.4 Conclusion on the choice of method 20
7.5 Consequences of implenting the new method 21

8 Evolution in stress over a period of 10 months 22

9 An empirical model for stress in supermirrors 23
9.1 Results 23
9.2 Changing the sputtering atmosphere 26

10 Discussion 26

11 Conclusion 26

References **28**

A *Gnuplot* script for calculating the curvature radius **30**

B Difference between the 1/R Method and the 12th Order Method **32**
B.1 How the fit works 32
B.2 Substrate curvature 32
B.3 The 1/R Method 33
B.4 The 12th Order Method 34

C The polynomial order **36**

D The coating on Romain Girard-Desprolet's samples. **37**

E Evolution in curvature over a period of 10 months **38**

F The Ti - NiV supermirror **39**

1 Motivation

Development in material science is strongly dependent on high flux neutron sources like the ones at the Institut Laue-Langevin [1] and the soon to come European Spallation Source [2]. Since the precision of the conducted experiments depends directly on the number of neutrons reaching the samples, enormous resources are spend on making these sources as powerful as possible. The invention of supermirrors for the guide tubes at these sites gives an increase of the net flux by a factor 2 or 3 for a vanishingly small price compared to building bigger reactors or spallation sources [1] [2]. The present largest limitation on supermirror construction is the peeling off due to the high amount of intrinsic stress in the multilayers making up the supermirror [5]. Therefore, a thorough research of the parameters influencing the stress is necessary in order to be able to eventually minimize it.

2 Introduction

The experimental proof of the wave nature of the neutron was of great interest after its discovery by Chadwick in 1932. The neutron's ability to perform Bragg diffraction was already shown in 1936 [8], but the real progress in neutron optics came with the first heavy water reactor, CP-3 in 1944, where it was shown that neutrons, as well as light, could be the origin of optical phenomena such as reflection [8].

At neutron research centres such as *ILL* [1] and *ESS* [2], high intensity neutron beams are generated for use in various experiments, for example studies of materials on a molecular or atomic scale. To minimize background radiation from the source and simply to get enough space for all the equipment, the experiments must be placed at some distance from the source. Therefore neutron guiding tubes are needed to transport the beam from the source to the experiments. To keep the neutrons in the guides, the guides are usually covered on the inside with natural abundance nickel or nickel 58 plates acting as mirrors by sub critical angle reflection due to a difference in refractive index.

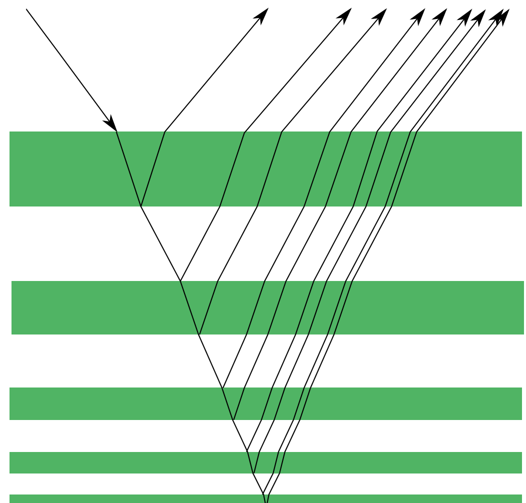

Figure 1: In a supermirror high reflectivity is obtained from continuous Bragg reflection from the depth-graded variation of the layer thickness in a multilayer.

The weakness of this guiding method is that the critical angle for the neutrons of interest is quite low, about $0.2°$ for a wavelength of 2Å [9]. To increase this angle, Mezei [10] proposed in 1976 to use Bragg diffraction from multilayer films in addition to the total internal reflection. These films consist of interchanging layers with different refractive indices, where the thickness of the layers varies throughout the structure. This gives a superposition of Bragg peaks in the reflection, which essentially increases the effective critical angle. This angle is proportional to the fourth root of the number of layers [11].

In the production of these new supermirrors it was however discovered that internal stress accumulates in the multilayer structures. This stress can be strong enough to rip the films from the substrate, thereby destroying the mirror [5]. In this project we will investigate how the physical parameters of the films influence the stress, in an attempt to be able to minimize it. This could in the longer term contribute

to the production of more effective mirrors, thus increasing the intensity of the neutron beams available for research.

3 Thermal neutron scattering

Since neutron scattering is the origin neutron optical effects, we will here give an outline of the necessary fundamental theory for understanding neutron optics. The scattering of neutrons origins from either an interaction with nuclear forces or by the interaction between the magnetic moment of the neutron and unpaired electrons. The simplest example is that of a neutron interacting with a bound nucleus situated at the origin. Since the wavelength of the thermal neutrons ($\sim 10^{-10}$ m) is much larger than the range of the nuclear forces which cause the scattering ($\sim 10^{-14}$–10^{-15} m), the scattered wave will be spherically symmetric [12, p. 7]. The incoming wave of neutrons can be represented by a plane wave at time zero

$$\psi_i = e^{ik_i z}, \tag{1}$$

and the scattered wave by a spherically symmetric wave function

$$\psi_f = -\frac{b}{r} e^{ik_f r}, \tag{2}$$

where b is the *bound nuclear scattering length*. The minus sign is chosen so a positive value of b corresponds to a repulsive potential [12, p. 8]. If the scattering length is a complex number, the imaginary part corresponds to absorption. We will here consider only real scattering lengths. Since the energy of a thermal neutron (~ 25 meV) is too small to change the internal energy of the nucleus, and the position of the nucleus is taken to be fixed, the neutron can not transfer any energy to the nucleus. The scattering will therefore be elastic.

3.1 Neutron scattering cross section

It is convenient to introduce the *cross section*, which describes the probability of a scattering event to happen. We will here deduce an expression for the cross section for a quantum mechanical system.

The partial differential cross section is defined as [12, p. 6]

$$\frac{d\sigma^2}{d\Omega dE_f} = \frac{\text{number of neutrons scattered per second into the solid angle } d\Omega \text{ in the direction } \theta,\, \phi \text{ with a final energy between } E_f \text{ and } E_f + dE_f}{\Phi d\Omega dE_f}, \tag{3}$$

where Φ is the flux of neutrons (number per unit area per time). Thus the dimension of the cross section, σ, is area. If we simply count all the neutrons scattered into a solid angle $d\Omega$ in the direction θ, ϕ we get the differential cross section

$$\frac{d\sigma}{d\Omega} = \frac{\text{number of neutrons scattered per second into the solid angle } d\Omega \text{ in the direction } \theta,\, \phi}{\Phi d\Omega}. \tag{4}$$

When we look at our simple example with the fixed nucleus, we can easily calculate the total cross section using the definitions of ψ_i and ψ_f, equations (1) and (2). From the definitions in figure 2 we can deduce that, if v is the velocity of the neutrons, the number of scattered neutrons passing the area dS per second is [12, p. 9]

$$v dS |\psi_f|^2 = v dS \frac{b^2}{r^2} = v b^2 d\Omega, \tag{5}$$

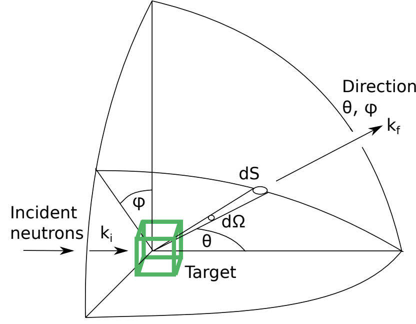

Figure 2: The geometry of a scattering experiment, after [12]. k_i and k_f are the neutron wave vectors before and after scattering, θ and ϕ the angular coordinates of the infinitesimal solid angle element $d\Omega$, and dS the area of $d\Omega$ at a distance r from the sample.

and the flux of incident neutrons is (*density* $\times$ *velocity*)

$$\Phi = |\psi_i|^2 v = v. \tag{6}$$

Using the definition (4), the differential cross section is easily calculated

$$\frac{d\sigma}{d\Omega} = \frac{vb^2 d\Omega}{\Phi d\Omega} = b^2, \tag{7}$$

and since b does not depend on θ and ϕ, the total cross section is

$$\sigma_{tot} = \int_{\text{all directions}} \left(\frac{d\sigma}{d\Omega}\right) d\Omega = 4\pi b^2. \tag{8}$$

We will now give a general description of a neutron with a wave number $\vec{k}_i$ and a wave function ψ_i incident on a scattering system in a state λ_i. The neutron interacts with the system via a potential V, and is scattered into a state described by the wave vector $\vec{k}_f$ and the wave function ψ_f. The system is likewise sent from the initial state λ_i to the final state λ_f. The scattering system is composed of N nuclei with the position vectors $\vec{R}_j$ $(j = 1, \ldots, N)$, and the position vector of the neutron is called $\vec{r}$. From the definition (4) we can write the differential cross section as [12, p. 11-13]

$$\left(\frac{d\sigma}{d\Omega}\right)_{\lambda_i \to \lambda_f} = \frac{1}{\Phi}\frac{1}{d\Omega} \sum_{\vec{k}_f \text{in } d\Omega} W_{\vec{k}_i,\lambda_i \to \vec{k}_f,\lambda_f}, \tag{9}$$

where $W_{\vec{k}_i,\lambda_i \to \vec{k}_f,\lambda_i}$ is the number of transitions per second from the state $\vec{k}_i, \lambda_i$ to the state $\vec{k}_f, \lambda_f$ which can be expressed using *Fermi's golden rule* [12, p. 11-12]

$$\sum_{\vec{k}_f \text{in } d\Omega} W_{\vec{k}_i,\lambda_i \to \vec{k}_f,\lambda_f} = \frac{2\pi}{\hbar} \rho_{\vec{k}_f} |\langle \vec{k}_f \lambda_f | V | \vec{k}_i \lambda_i \rangle|^2 \tag{10}$$

where $\rho_{\vec{k}_f}$ is the density of final states, i.e. the number of final momentum states per unit energy in $d\Omega$ around $\vec{k}_f$. The matrix element is given by

$$\langle \vec{k}_f \lambda_f | V | \vec{k}_i \lambda_i \rangle = \int \psi_f^* \chi_{\lambda_f}^* V \psi_i \chi_{\lambda_i} d\vec{R} d\vec{r}, \qquad d\vec{R} = d\vec{R}_1 d\vec{R}_2 \ldots d\vec{R}_N, \tag{11}$$

with χ_{λ_i} and χ_{λ_f} being the wave functions of the states λ_i and λ_f.

Adopting box normalisation and combining equation (4) with the expression for the incident neutron flux (*density* $\times$ *velocity*)

$$\Phi = \frac{1}{L^3}\frac{\hbar}{m}k_i, \tag{12}$$

we obtain an expression for the differential cross section

$$\left(\frac{d\sigma}{d\Omega}\right)_{\lambda_i\to\lambda_f} = \frac{k_f}{k_i}\left(\frac{m}{2\pi\hbar^2}\right)^2 |\langle\vec{k}_f\lambda_f|V|\vec{k}_i\lambda_i\rangle|^2 \tag{13}$$

where

$$\langle\vec{k}_f\lambda_f|V|\vec{k}_i\lambda_i\rangle = \int e^{-i\vec{k}_f\cdot\vec{r}}\chi^*_{\lambda_f}Ve^{i\vec{k}_i\cdot\vec{r}}\chi_{\lambda_i}d\vec{R}d\vec{r} \tag{14}$$

which was what we wanted to deduce.

3.2 Fermi pseudo potential

In neutron optics the interaction between neutron and matter can be expresed in terms of the Fermi pseudopotential $V(\vec{r})$ which we will calculate here. To do that, we return again to our simple example with the fixed nucleus in the origin, i.e. $j = 1$, $\vec{R}_1 = 0$, and $\lambda_f = \lambda_i$. We know that the nuclear potential $V(\vec{r})$ is short range so we can approximate it by $V(\vec{r}) = a\delta(\vec{r})$ for the matrix element in (13) to be calculated [12, p. 15]

$$\langle\vec{k}_f\lambda_f|V|\vec{k}_i\lambda_i\rangle = \int \chi^*_{\lambda_f}\chi_{\lambda_i}d\vec{R}_1 \int V(\vec{r})e^{i(\vec{k}_i-\vec{k}_f)\cdot\vec{r}}d\vec{r} \tag{15}$$

$$= \int a\delta(\vec{r})e^{i(\vec{k}_i-\vec{k}_f)\cdot\vec{r}}d\vec{r} = a. \tag{16}$$

Inserting this result in the expression for the differential cross section (13), we get

$$\frac{d\sigma}{d\Omega} = \left(\frac{m}{2\pi\hbar^2}\right)^2 a^2 \tag{17}$$

since the fixed nucleus and low thermal neutron energy implies elastic scattering so $k_f = k_i$. If we compare this with the result from (7), we obtain an expression for the potential $V(\vec{r})$

$$V(\vec{r}) = \frac{2\pi\hbar^2}{m}b\delta(\vec{r}) \tag{18}$$

which is known as the Fermi pseudopotential. When having n bound nuclei, we get the potential

$$V(\vec{r}) = \frac{2\pi\hbar^2}{m}\sum_{j=1}^{n} b_j\delta(\vec{r}-\vec{R}_j) = \frac{2\pi\hbar^2}{m}b(\vec{r}), \tag{19}$$

$$b(\vec{r}) \equiv \sum_j b_j\delta(\vec{r}-\vec{R}_j). \tag{20}$$

Here b_j is the bound scattering length of the jth atom and $\vec{R}_j$ its position, and $b(\vec{r})$ is the bound scattering length density. We can for a monatomic system express the mean bound scattering length density, using the bound coherent scattering length $b_c \equiv \langle b_j\rangle$ and the nucleus number density $\rho(\vec{r})$, as [13, p. 54]

$$\langle b(\vec{r})\rangle = b_c\langle\rho(\vec{r})\rangle. \tag{21}$$

3.3 Coherent scattering and neutron optics

Scattering is said to be coherent in an absolute sense if the scattered waves interfere with the incident wave [13, p. 49]. Since this is the origin of all optical phenomena, it is essentially only the absolute coherent scattering that we will consider here.

The scattering lengths vary slightly due to the different directions of the spins of the nuclei, the different isotopes in the material, and the presence of impurities. It is however only the mean value $\langle b \rangle$ that gives rise to coherent scattering [12, p. 22].

It can be shown that the neutron wave from coherent scattering is described by a one body Schrödinger equation [13, p. 53]

$$\left\{ -\frac{\hbar^2}{2m}\vec{\nabla}^2 + v(\vec{r}) \right\} \psi(\vec{r}) = E\psi(\vec{r}). \tag{22}$$

The optical potential $v(\vec{r})$ represents the effective interaction of the neutron with the media, and can be calculated averaging over all the nucleus potentials (19) [13, p. 55-56]

$$v(\vec{r}) = \left\langle \sum_j \frac{2\pi\hbar^2}{m} b_j \delta(\vec{r} - \vec{R}_j) \right\rangle = \frac{2\pi\hbar^2}{m} \langle b(\vec{r}) \rangle. \tag{23}$$

This is an approximation that only holds when the wavelength of the neutrons is much too large to make Bragg reflection in the crystal layers [13, p. 56]. This is equivalent to a small grazing incidence angle, as seen from Bragg's law

$$n\lambda = 2\delta \sin\theta, \tag{24}$$

where n is a natural number, λ is the neutron wavelength, δ is the distance between the crystal layers, and θ is the grazing angle of incidence. Since we are concerned with neutrons getting Bragg reflected from the film interfaces which have at least 10 times the distance between them, the approximation holds.

In the situation where the atoms are confined in a volume V, the number density $\rho(\vec{r})$ reduces to

$$\rho(\vec{r}) = \begin{cases} \rho & \text{inside } V \\ 0 & \text{outside } V \end{cases}. \tag{25}$$

The optical potential can now be written as

$$v(\vec{r}) = \begin{cases} v_0 & \text{inside } V \\ 0 & \text{outside } V \end{cases}, \tag{26}$$

where, from equations (23), (21), and (25),

$$v_0 = \frac{2\pi\hbar^2}{m} \rho b_c. \tag{27}$$

The solution to equation (22) can be written as a superposition of plane waves. The magnitudes of the neutron wave vector inside the material k and in vacuum k_0 are determined by the incident neutron energy

$$E = \frac{\hbar^2 k^2}{2m} + v_0 = \frac{\hbar^2 {k_0}^2}{2m}. \tag{28}$$

3.4 Index of refraction

The interaction of a neutron wave with a material can be described by an index of refraction [13, chap. 3.1]

$$n = \frac{k_1}{k_0}. \tag{29}$$

It can now easily be deduced from equations (28) and (27) that

$$n^2 = 1 - \frac{v_0}{E} = 1 - \frac{4\pi}{k_0^2}\rho b_c = 1 - \frac{\lambda_0^2}{\pi}\rho b_c, \tag{30}$$

where λ_0 is the neutron wavelength in vacuum. This can be generalised to the case of an interface between two media 1 and 2, where the relative index of diffraction is defined as

$$n = \frac{k_1}{k_2} = \frac{n_1}{n_2}, \tag{31}$$

and can be expressed in the limit where E is much bigger than v_1 and v_2, as

$$n^2 = 1 - \frac{1}{E}(v_1 - v_2) = 1 - \frac{\lambda^2}{\pi}(\rho_1 b_1 - \rho_2 b_2). \tag{32}$$

4 Reflection

4.1 Critical angle

Due to the continuity of the wave function and its derivative, the critical angle for a neutron interacting with a mirror can be calculated using Snell's law from classical optics [13, chap. 3.1]. It relates the angles of incidence and refraction when a wave passes through a boundary between two media. In neutron optics it is, due to the small angles, more naturel to use grazing angles, and Snell's law is expressed in terms of the cosine to the angles

$$n_1 \cos\theta_1 = n_2 \cos\theta_2. \tag{33}$$

The grazing critical angle for an interface between two materials, θ_c, is defined as the smallest angle for which there is a solution to Snell's law. For angles below this value, nothing will pass the interface, so there is total internal reflection. The grazing critical angle can easily be deduced from equations (33) and (30)

$$\begin{aligned} \cos\theta_c &= n \Rightarrow \\ \sin\theta_c &= \lambda\sqrt{\frac{\rho b}{\pi}} \end{aligned} \tag{34}$$

for positive b. In the same way equation (32) gives

$$\sin\theta_c = \lambda\sqrt{\frac{\rho_1 b_1 - \rho_2 b_2}{\pi}}. \tag{35}$$

For thermal neutron wavelengths $\theta_c \leq 1°$ which makes the approximation $\sin\theta_c \approx \theta_c$ valid.

4.2 Reflection from a multilayer

Now knowing that the interaction between the neutrons and the mirror can be described by an optical potential, we will here outline how the reflectivity of a multilayer system is calculated. When considering a plane wave propagating in the (z, x) plane incident on a planar surface with stratification in the z direction, the potential only depends on the z variable. Therefore the influence of the mirror on the wave is described by

$$\frac{d^2\psi}{dz^2} + q^2\psi = 0. \tag{36}$$

Here q is the component of the wave vector normal to the interface, i.e. in the z-direction. Thus $q = k\cos\theta$, where θ is the grazing incidence angle. q is for each layer uniquely determined by the incoming wave vector and the optical potential by equation (28). The reflection and transmission coefficients r and t are defined in terms of the solution to (36) with q_a and q_b being respectively the normal component of the wave vector before and after the stratified medium

$$e^{iq_a z} + re^{-iq_a z} \leftarrow \psi \rightarrow te^{iq_b z}. \tag{37}$$

To calculate the reflectivity of a neutron wave interacting with a stratified medium, continuity of the wave function and its first derivative ψ' over each boundary is imposed. In general, when given a one layer medium with a constant optical potential v_0 and thickness δ, it can be shown that [14, chap. 12-2]

$$\begin{pmatrix}\psi_b \\ \psi'_b\end{pmatrix} = \boldsymbol{M}\begin{pmatrix}\psi_a \\ \psi'_a\end{pmatrix} = \begin{pmatrix}\cos(q\delta) & \frac{1}{q}\sin(q\delta) \\ -q\sin(q\delta) & \cos(q\delta)\end{pmatrix}\begin{pmatrix}\psi_a \\ \psi'_a\end{pmatrix}. \tag{38}$$

When having af succession N of stratified layers with different thickness δ_n and optical potential v_{0n} (which implies different q_n), the characteristic matrix of the whole medium is

$$\boldsymbol{M} = \begin{pmatrix}m_{11} & m_{12} \\ m_{21} & m_{22}\end{pmatrix} = \boldsymbol{M}_N\boldsymbol{M}_{N-1}\cdots\boldsymbol{M}_n\cdots\boldsymbol{M}_2\boldsymbol{M}_1, \tag{39}$$

where the characteristic matrix $\boldsymbol{M}_n$ of the n'th layer is given by

$$\boldsymbol{M}_n = \begin{pmatrix}\cos(q_n\delta_n) & \frac{1}{q_n}\sin(q_n\delta_n) \\ -q_n\sin(q_n\delta_n) & \cos(q_n\delta_n)\end{pmatrix}. \tag{40}$$

It can be shown that the reflection and transmission coefficients are expressed by [14, chap. 12]

$$r = e^{2iq_a z_1}\frac{q_a q_b m_{12} + m_{21} - iq_b m_{11} + iq_a m_{22}}{q_a q_b m_{12} - m_{21} + iq_b m_{11} + iq_a m_{22}}, \tag{41}$$

$$t = e^{i(q_a z_1 - q_b z_{N+1})}\frac{2iq_a}{q_a q_b m_{12} - m_{21} + iq_b m_{11} + iq_a m_{22}}. \tag{42}$$

In terms of r and t the reflectivity and transmittance, which are the proportions of the energy reflected or transmitted, are given by

$$R = |r|^2, \qquad T = \frac{q_b}{q_a}|t|^2. \tag{43}$$

For a supermirror, the reflection for angles above the critical angle comes from the stratification of layers. For a film with layers of constant thickness, the reflectivity is optimized when

$$q\delta = \frac{\pi}{2}. \tag{44}$$

This is equivalent to solving Bragg's law (24) with $n = 1$ and a 180° phase shift at one of the interfaces. The result is a Bragg peak for the value of q fullfilling (44), for which the reflectivity can be made arbitrarily good by adding more layers. When constructing supermirrors, a graduation in the thickness of the layers is made to generate Bragg peaks for multiple q-values, i.e. multiple incidence angles. Because the Bragg peaks have a finite width, it is possible to create mirrors where all the peaks add up to a continuous zone of almost perfect reflectivity. Thus it is possible to obtain a much higher critical angle of close to total reflection.

There are several algorithms for determining the best distribution of layer thickness, the most commonly used being that of Hayter and Mook [11]. The reflectivity of a supermirror is always compared to that of a normal critical angle mirror made of natural abundance nickel, and expressed in terms of its m value

$$\theta_{SM} = m\theta_{Ni}, \tag{45}$$

where θ_{SM} is the angle of maximum reflection of the supermirror, and θ_{Ni} is the critical angle of nickel. m increases with a decreasing thickness of the thinnest layers, and thus an increasing number of layers. The number of layers in the mirror can be shown to be proportional to m^4 [9], when using the algorithm of Hayter and Mook [11].

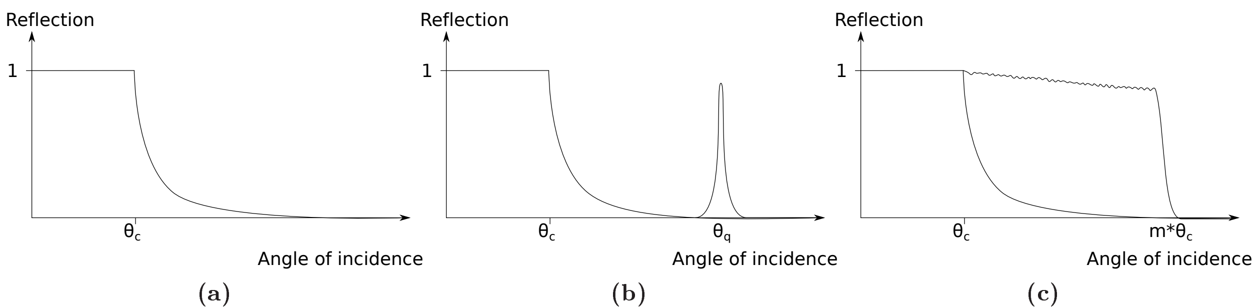

Figure 3: Neutrons are reflected from interfaces between materials with different indices of refraction. When the index of refraction of the incidence material is higher than the index of refraction of the mirror, the neutrons are completely reflected up to a critical angle θ_c, as shown in figure 3a. A multilayer consisting of a number of identical bilayers will make an incident neutron beam diffract, and the reflected waves interfere constructively for an incident angle given by Bragg's law (44). An example of such a diffraction peak, called a Bragg peak, is shown in figure 3b. A graduation of thickness generates multiple Bragg peaks. The summation of Bragg peaks results in a zone of nearly total reflection. Neutron supermirrors are characterized by their reflectivity and their m value. The m-value describes the range of the supermirror as the number of times the maximum angle of reflection is bigger than θ_c for natural abundance nickel, as shown in figure 3c.

5 Thin film stress

As we have seen in the previous section, the reflectivity and m-value is limited by the number of layers. Unfortunately thin films are subjected to internal stress, and the accumulation of layers leads to a corresponding accumulation of stress. When the force per unit width between the downmost layer and the substrate exceeds the binding strength between the to materials, the film will peel of. This is one of the biggest limitations on supermirror construction [5].

The stress is mainly composed of a thermal part and one related to the film structure and growth conditions [15]. When the materials of the film and the substrate have different thermal expansion rates, the difference in the production temperature and room temperature will make them expand differently. Because the materials are constrained by each other, this will lead

to stress. This stress can in most cases be predicted and calculated. The other part however, the intrinsic stress, is not quite as well understood. When the film grows on the substrate, its microstructure may differ from the one it usually has. It will nevertheless try to relax into its normal state, but because expansion or contraction is inhibited by the binding to the substrate, stress will occur.

5.1 Aspects of elasticity theory

Before the derivation of the Stoney equation for film stress in section 5.2, we will here introduce some fundamental elasticity theory. The subject of elasticity deals with the behavior of substances who have the property of recovering their size and shape when the forces producing deformations are removed. This behavior is described by three quantities:

Strain: The relative deformation of the material, usually denoted by the symbol ϵ. If for example a steel bar of 1 meter expands by 5 millimeters, $\epsilon = 0.005$. To be able to describe not only expansion and contraction, but also shear, one defines the second order strain tensor ϵ_{lm}, with l and m being one of the three coordinate axes. If one observes a deformation δu_l in the l direction when moving δx_m in the m direction, $\epsilon_{lm} = \delta u_l/\delta x_m$. Here u denotes a displacement from the relaxed state in units of length. $\delta u_l/\delta x_m$ would however also be different from zero if we rotated the material. There is thus a need for a definition of strain that is independent of rigid rotation. It can be shown [16] that

$$\epsilon_{lm} = \frac{1}{2}\left(\frac{\delta u_l}{\delta x_m} + \frac{\delta u_m}{\delta x_l}\right) \tag{46}$$

satisfies this condition. From here it is also seen that ϵ_{lm} is a symmetric tensor, i.e. $\epsilon_{lm} = \epsilon_{ml}$, and that it as such only has 6 different components.

Stress: A measure of the internal forces due to the deformation. More precisely is it the force per unit area needed to induce a certain strain. For each plane cut through the wafer, there can be a force in any direction between the material on each side of the plane. Therefore, the stress must be a tensor: $\sigma_{ik} = \delta F_i/\delta A_k$. It is a symmetric tensor too, i.e. $\sigma_{ik} = \sigma_{ki}$, since the torque on an infinitesimal mass element must decrease at least as fast as the moment of inertia when the size of the element goes towards zero [16]. Thus it also only has six different components.

Elasticity tensor λ_{iklm}: In linear elasticity theory, which we consider here, the stress and strain are related by

$$\sigma_{ik} = \sum_{l=1,m=1}^{3,3} \lambda_{iklm}\epsilon_{lm}. \tag{47}$$

λ_{iklm} is a fourth order tensor, since each stress component is a priori capable of contributing to any of the strain components. However, since the stress and strain tensors only have six different components, λ_{iklm} can at most have 36 different components.

If the material is completely isotropic, λ_{iklm} only has two linearly independent components, which we can express in terms of Young's modulus E and Poisson's ratio ν. They are defined as following

$$\sigma_{ii} = E\epsilon_{ii}, \tag{48}$$

$$\epsilon_{jj} = -\nu\epsilon_{ii}, \tag{49}$$

if there is only stress in the ii direction. For an isotropic material, shear can be expressed as a combination of expansion and compression [16]. σ_{ik} and ϵ_{lm} are in general fields that depend on the position. λ_{iklm}, however, is a specific constant for a given material.

5.2 Determining thin film stress by substrate curvature measurement

To ensure mechanical equilibrium, stressed thin films have a tendency to bend the substrate. G. G. Stoney was the first to derive a formula relating the film stress σ_f to the radius of curvature R of the substrate as a result of studying how deposited iron films bend steel strips [6]. Mechanical equilibrium requires that the sum of the forces and bending moments within the substrate and the film vanish.

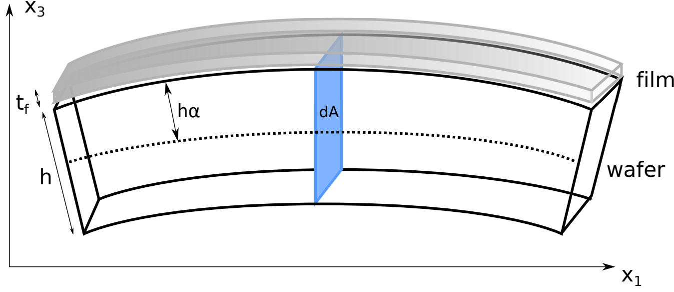

Figure 4: A figure of the substrate coated by a thin film orientated along the x_1 direction. The bending induced by the stress in the film is in the x_3 direction. On the figure t_f denotes the thickness of the film, h the thickness of the substrate, dA an area element perpendicular to the x_1 direction and $h\alpha$ the distance from the neutral plane, where there is neither contraction nor expansion, to the film.

If one imagines a beam oriented along the x_1 direction that bends in the x_3 direction as on figure 4, these conditions are ensured if

$$F = \int \sigma_{11} dA + F_{film} = 0, \tag{50}$$

$$M = \int \sigma_{11} x_3 dA + M_{film} = 0 \tag{51}$$

where dA is an area element perpendicular to the x_1 direction, σ_{11} is the stress in the film, and F_{film} and M_{film} are the force and bending moment induced by the film. From here Stoney deduced

$$\sigma_f t_f = \frac{Eh^2}{6R} \tag{52}$$

where t_f is the thickness of the film, h is the thickness of the substrate, and E is Young's modulus. Even though the strip is considerably longer than wide, Stoney's assumption of uni-axial stress is in general not valid, due to the fact that the width of the strip is still much larger than the thickness. A revised formula takes the biaxial stress into account, expressing the elastic behavior of the strip not only in terms of Young's modulus but also Poisson's ratio:

$$\sigma_f t_f = \frac{Eh^2}{(1-\nu)6R}. \tag{53}$$

This is the Stoney equation for a two dimensional elastically isotropic substrate. A typical example of a substrate is a silicon wafer with the dimensions $50 \times 10 \times 1\text{mm}^3$. We define the three coordinate axes x_1, x_2, and x_3 as being parallel to the length, the width and the thickness directions of the wafer respectively. A two dimensional substrate will bend spherically due to the isotropy and homogeneity of the wafer and the film in the x_1 and x_2 directions. The curvature radius is thus independent of where and in which direction it is measured.

5.3 The Stoney equation for the silicon (111) wafer

Since silicon is an anisotropic material with a diamond like cubic crystal structure, a modified Stoney equation has to be deduced from the conditions given in equations (50) and (51). We will try to outline the calculation here [17].

At first we must calculate λ_{iklm}. In the case of a cubic crystal structure, λ_{iklm} has only got three distinct elements, a fact which can be deduced from the following two observations:

1. Every element containing an uneven number of a certain index, for example λ_{xxxz}, has to be zero to avoid violation of reflection symmetry.

2. Any change of the axes should yield the same values, for example $\lambda_{xyxy} = \lambda_{xzxz}$, due to symmetry of parity and 120° rotation about the (111) axis [18].

The remaining elements will be renamed as following

$$\lambda_{xxxx} = c_{11} \tag{54}$$

$$\lambda_{xxyy} = c_{12} \tag{55}$$

$$\lambda_{xyxy} = 2c_{44} \tag{56}$$

which makes it possible to write the relation (47) as

$$\begin{pmatrix} \sigma_{11} \\ \sigma_{22} \\ \sigma_{33} \\ \sigma_{23} \\ \sigma_{13} \\ \sigma_{12} \end{pmatrix} = \begin{pmatrix} c_{11} & c_{12} & c_{12} & & & \\ c_{12} & c_{11} & c_{12} & & & \\ c_{12} & c_{12} & c_{11} & & & \\ & & & c_{44} & & \\ & & & & c_{44} & \\ & & & & & c_{44} \end{pmatrix} \cdot \begin{pmatrix} \epsilon_{11} \\ \epsilon_{22} \\ \epsilon_{33} \\ 2\epsilon_{23} \\ 2\epsilon_{13} \\ 2\epsilon_{12} \end{pmatrix} . \tag{57}$$

c_{11}, c_{12} and c_{44} are called the elastic stiffness constants which have been determined experimentally [17]. The final result will however for simplicity be expressed in terms of the compliance matrix s_{ij} which is the inverse of c_{ij}. We have now found the relation between stress and strain in the coordinate system of the crystal axes, but in fact we want it for the wafer plane. We define e_1, e_2 and e_3 as unit vectors being parallel to x_1, x_2 and x_3 respectively. In the crystal basis they are

$$e_1 = \begin{pmatrix} 1/\sqrt{2} \\ -1/\sqrt{2} \\ 0 \end{pmatrix}, \qquad e_2 = \begin{pmatrix} 1/\sqrt{6} \\ 1/\sqrt{6} \\ -2/\sqrt{6} \end{pmatrix}, \qquad e_3 = \begin{pmatrix} 1/\sqrt{3} \\ 1/\sqrt{3} \\ 1/\sqrt{3} \end{pmatrix}. \tag{58}$$

From these the elastic stiffness matrix of the wafer system can be deduced by transformation.

Having found the relation between stress and strain, we now proceed to relating the strain to the curvature and introducing the conditions of force equilibrium. We assume that the displacement in the plane of the wafer is negligible, ($u_1 = 0$ $u_2 = 0$), and that its perpendicular component is isotropic and given by

$$u_3 = a(x_1^2 + x_2^2) \tag{59}$$

which is a Taylor expansion of the spherical curvature. u_i denotes a displacement from the relaxed state in the i direction. The curvature radius is related by

$$a = \frac{1}{2R}, \tag{60}$$

and the strain is, from equation (46)

$$\epsilon_{ij} = \frac{1}{2}\left(\frac{\partial u_i}{\partial x_j} + \frac{\partial u_j}{\partial x_i}\right). \tag{61}$$

Since mechanical equilibrium is assumed to be reached, and the stress is supposed to be homogeneous in the e_1 and e_2 directions,

$$\sigma'_{13} = \sigma'_{23} = \sigma'_{33} = 0. \tag{62}$$

The ' denotes that the stress is along the wafer coordinates e_1, e_2, and e_3 and not the crystal axes from equation (57). By simple algebra and differentiation the following can be deduced

$$\begin{pmatrix} \sigma'_{11} \\ \sigma'_{22} \\ \sigma'_{33} \\ \sigma'_{23} \\ \sigma'_{13} \\ \sigma'_{12} \end{pmatrix} = -2ax_3 \frac{6}{4s_{11} + 8s_{12} + s_{44}} \begin{pmatrix} 1 \\ 1 \\ 0 \\ 0 \\ 0 \\ 0 \end{pmatrix}. \tag{63}$$

In this formula the zero of the x_3-axis is situated at the plane inside the wafer where there is neither contraction nor expansion. If we call the distance from the neutral plane to the film αh as seen in figure 4, a from definition (59) can be found from the equilibrium conditions (50) and (51)

$$\int_{h(\alpha-1)}^{\alpha h} \sigma'_{11} dx_3 + \sigma_f t_f = 0 \tag{64}$$

$$\int_{h(\alpha-1)}^{\alpha h} x_3 \sigma'_{11} dx_3 + \alpha h \sigma_f t_f = 0. \tag{65}$$

The solution to these equations together with (63) and (60) gives us the final result

$$\sigma_f t_f = \left(\frac{6}{4s_{11} + 8s_{12} + s_{44}}\right) \frac{h^2}{6R} = 2.291 \cdot 10^{11} \mathrm{Nm}^{-2} \cdot \frac{h^2}{6R} \tag{66}$$

of which the last equality is based on experimental results [17].

6 Experimental setup

Our goal is to make a model for how the stress depends on the growth parameters. For this we have deposited multilayer films by magnetron sputtering on silicon (111) wafers. The radius of curvature induced by the film stress is measured with a Twyman-Green interferometer from the company *FISBA Optik*, belonging to the Mirror and Metrology Laboratory [3] at the *ESRF* [4]. The curvature radius can together with the Stoney equation (66) be used to calculate the stress.

6.1 Choice of substrate

We have to make sure that the Stoney equation is valid for our type of film and substrate. The necessary conditions are:

1. The substrate has to be elastically isotropic in the plane of the wafer. This ensures that the bending can be described by one single radius of curvature. The silicon (111) fulfills this condition, despite that it is not generally isotropic [17].

2. The substrate must be much thicker than the film to ensure the validity of equations (64) and (65).

3. The bending displacement of the substrate should be big enough to be measured but small enough for the approximation (59) to be valid. A too big bending may also lead to a nonspherical curvature, i.e. the wafer will bend cylindrically [19].

4. To avoid boundary effect, the thickness of the wafer has to be much smaller than its width and length.

For our measurements, we use silicon (111) wafers with the dimensions $50 \times 10 \times 1$ mm as substrates. With a film thickness at less than 10 μm and a curvature radius above 10 m, the conditions 1-4 have been shown to be satisfied [19].

6.2 Thin film deposition by magnetron sputtering

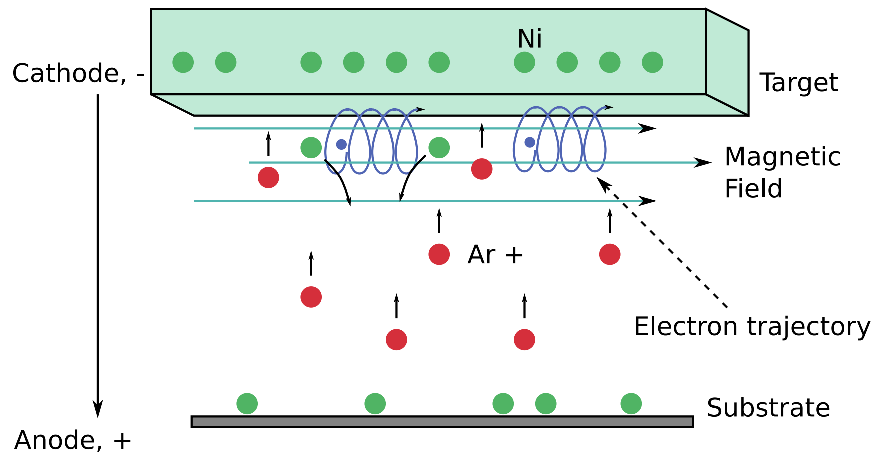

Figure 5: Magnetron Sputtering, as described in section 6.2. The green box is the target made of nickel, and the green circles are individual nickel atoms. The grey plate is the substrate with the beginning film growth. The red circles are argon ions created from and accelerated by the potential difference between the substrate and the target, hitting each other and the target while releasing nickel atoms and electrons. The electrons follow the dark blue helical path around the light blue magnetic field.

The thin films that we investigate are deposited by magnetron sputtering, see figure 5. The basic principle behind sputtering consists of having a target plate bombarded by energetic ions causing expulsion of target atoms which then condensate on a substrate and form a thin film. The projectile particles are argon atoms that are ionized by the phenomenon glow discharge where a voltage difference between the target and the substrate makes them act as a cathode and an anode. The efficiency of the sputtering increases with an increasing number of argon ions. When the target is bombarded, a small amount of the atoms are released and a number of free electrons will therefore also be released. A magnetic field is aligned parallel to the target surface, forcing the trajectory of these secondary electrons together with the electrons from the ionized argon to be in the vicinity of the target. This enhances the probability of ionizing electron-argon collisions which means increased ion bombardment and hence higher deposition rates [20]. The film thickness can be determined by calibrating the voltage difference and the time the substrate spends under the target.

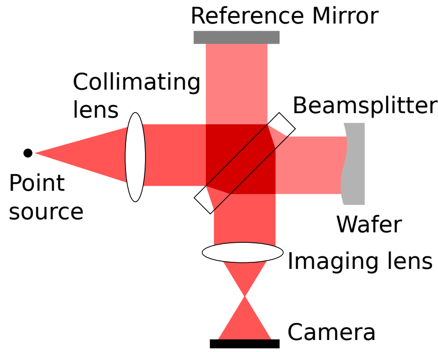

Figure 6: The Twyman-Green interferometer. A laser beam is divided in two by a beam splitter. One beam is reflected by a reference mirror, the other by the sample. Afterwards they are reassembled at the beam splitter and an interference pattern is collected by the camera.

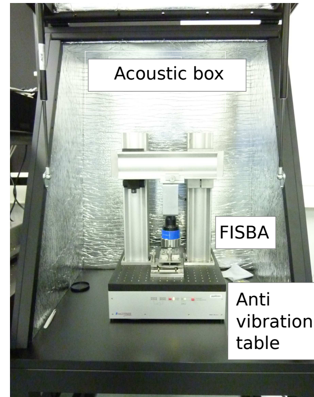

Figure 7: In the clean room the interferometer is placed on the anti vibration table in an acoustic box. The lid of the box can be closed so it is almost airtight.

6.3 The *FISBA* Twyman-Green interferometer

A Twyman-Green interferometer is a variant of the normal Michelson interferometer, as seen in figure 6. The light enters at the left and gets split by the beam splitter, reflected by the reference mirror and the sample, reassembled at the beam splitter, and finbally collected at the camera. The image seen by the camera is a fringe pattern determined by the distance travelled by the two beams. Let λ be the wavelength of the laserbeam, and n a natural number. If the optical path length of one beam is λn longer than the other's, they will interfere constructively, while the interference will be destructive, if the difference is $\lambda n + \lambda/2$. As any surface deviation of the sample results in a changed optical path length, it will also give a changed fringe pattern. To get the highest precision, the tilt of the wafer is adjusted to the least amount of fringes possible. When taking the measurements, the reference mirror is moved in small steps changing the optical path length. For each step a new interference pattern is found, and when combining them a computerprogram called *µShape* [21] calculates the surface structure. There are several parameters that can be changed, of which the most important are the number of pictures taken for each position of the wafer and the number of times the entire process is repeated.

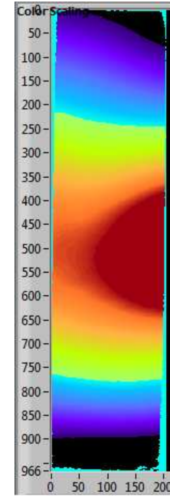

Figure 8: An example of a surface topography image from *Labview*. The units on the axes are pixels. The red areas correspond to a high x_3-value and the black areas to a low x_3-value.

Since the total height difference from one spot to another on the wafer is never above 3 μm, a high stability of the setup is necessary to ensure measurement reproducibility. This is the reason for placing the interferometer in a clean room, since dust grains on the sample disrupt the interference pattern. It is also of great importance to reduce vibrations in the setup. Normal speech can make the interferometer incapable of measuring anything, so certain measures have been taken to get the most stable measurements. First of all the interferometer has been placed on an active anti vibration table which uses piezoelectric crystals to cancel vibrations. This makes the fringe pattern independent of ground vibrations, for example from people walking in the room. The table is furthermore placed inside an acoustic box with isolation against noise and air convection, as seen in figure 7.

The data are used by *µShape* [21] to make a contour plot of the surface topography, as seen in figure 8. To extract a profile on this image, along which we can measure the

curvature, we use a *Labview* program written by the Mirror and Metrology Group at *ESRF* [3] . This program shows the contour plot from *µShape*, and has two cursors, between which the surface profile can be extracted, as seen in figure 8.

7 A new method for calculating the effective curvature radius

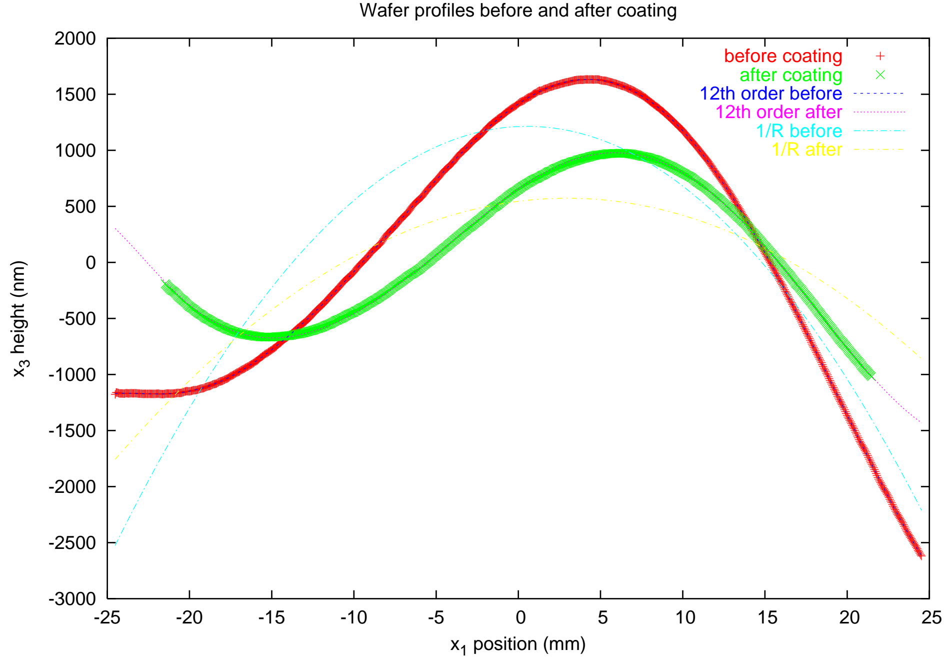

Figure 9: The curvature profiles of the same wafer before and after coating. The red points are the data from the profile before coating and the green points are from after coating. The dark blue and purple lines are the corresponding fits using the 12th Order Method, as described in section 7.2. The light blue and yellow lines are the corresponding second order fits with the 1/R Method. Data from [22].

To use the Stoney equation we have to have a measure of the curvature radius induced by the film, the *effective curvature radius*, $R_{effective}$. As seen in figure 9, this curvature can not be extracted solely from the surface profile of the wafer after coating, since the bending induced by the film is of the same order of magnitude as the initial curvature of the wafer. We expect the bending from the film to be superimposed on the initial curvature profile. Therefore it can be found by subtracting the profile of the wafer before coating from the one after coating.

The first part of our project was to evaluate the existing method for determining $R_{effective}$, that in the following will be called the *1/R Method*.

7.1 The 1/R Method

If one fits a second order polynomial to a spherical surface profile, the curvature radius will be inversely proportional to the second order coefficient, as seen in equation (60). As a parabola in principle can be fitted to any data set, it is possible to assign a curvature radius to any surface profile. This is exploited in the 1/R Method where the inverse of the effective curvature radius is

$$\frac{1}{R_{effective}} = \frac{1}{R_{after}} - \frac{1}{R_{before}}. \tag{67}$$

R_{before} and R_{after} are the curvature radii of the wafer before and after coating calculated from equation (60) after having fitted a second order polynomial to each surface profile.

One instantly sees that a parabola is not a very good approximation to either of the curves in figure 9. The radius would strongly depend on where on the wafer we measure it. It would, for example, be negative if measured on the interval [0:15], while positive towards each end. This is especially a problem since the interferometer is not capable of measuring the entire wafer if the curvature is too high, so one has to choose where one wants to take the measurement. In that case the 1/R Method does not give a consistent result.

This was the motivation for changing to a method where the complex form of the wafer before coating is taken into consideration. This new method will be called the *12th Order Method*.

7.2 The 12th Order Method

Instead of just subtracting the curvature radii, we thought that it would be better to subtract the entire surface profile of the wafer before coating from the one after coating, and then calculate the effective curvature radius from what remains. This was done with the *Gnuplot* script shown in appendix A. The method works as following: First we fit a 12th order polynomial to the profile before coating. All 13 parameters are determined by this fit, and in practice we get an almost perfect fit to the data set. This is the dark blue line in figure 9. We now have a 12th order polynomial with fixed parameters which precisely models the curvature profile of the wafer before coating, the background. Now we want to make a fit for the curvature induced by the film. To do this, we use the idea that the film induces a parabolic curvature on top of the background curvature profile. In practice we fit the profile of the wafer after coating to the sum of the background polynomial and a second order polynomial. All three parameters of the second order polynomial are free to be fitted, but the parameters in the background 12th order polynomial are fixed from the first fit, except that we introduce a free deplacement parameter so the zero of the function can move arbitrarily on the x-axis. I.e. we fit $f(x - x_0) + b_0 + b_1 x + b_2 x^2$ to the surface profile after coating via x_0, b_0, b_1, b_2, where $f(x)$ is the fixed background polynomial.

Essentially the fit subtracts the initial curvature profile from the final, taking into account that the length of the profile is not necessarily the same for the wafer before and after coating and that there can be a small displacement between the two profiles. The b parameters then model the effective curvature. We see that b_2 corresponds to a in equation (60).

A support for the 12th Order Method is that the second fit, the purple line on figure 9, is remarkably good when considering that the higher degree parameters were determined by a fit to the background wafer profile. This is a strong motivational factor for trying the 12th Order Method, and one could therefore be convinced to believe that the 1/R Method should never give a good result. We have however showed analytically in appendix B that the two methods actually give exactly the same curvature radius, when one is capable of tracing the surface profile along the exact same line on the wafer before and after coating. This result is however of little practical importance, since it is impossible to do so. We have examined the importance of the order of the fit in the appendix C.

7.3 Improved precision with the 12th Order Method

We have conducted several tests to find the difference in precision between the two methods. At first we reexamined measurements on iron - silicon multilayers taken by Romain Girard-Desprolet [22], a student who worked on a previous stress measurement project in the Multilayer laboratory. The composition of layers is shown in appendix D. Afterwards we also examined the precision our own samples.

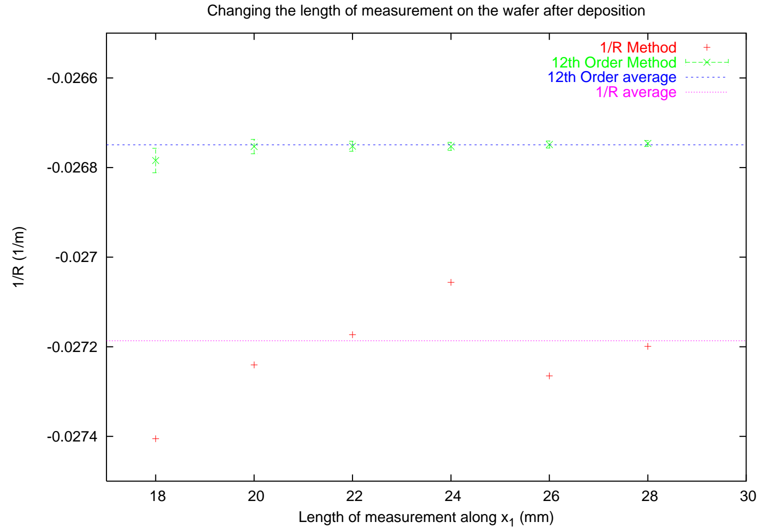

Figure 10: How the length of the traced surface profile changes the measured curvature radius. The red points are the inverse curvature radius calculated with the 1/R Method and the green points are the inverse curvature radius calculated with the 12th Order Method as a function of measurement length. The errror bars on the green points are due to fitting uncertainty. Further details can be found in section 7.3.1. Data from [22].

7.3.1 Different lengths

As we have mentioned in section 7.2, the essential difference between the two methods is a priori how stable they are regarding changing the length of the traced surface profile. This is presented in figure 10.

The surface profiles used were not the same for the two methods in order to implement both methods correctly. For the 1/R Method we traced surface profiles with the same length on both the before and after image of the wafer, as prescribed in section 7.1, and centered them around the middle of the wafer in the x_1 direction. When using the 12th Order Method, we traced a long line of about 40 mm on the wafer before coating, while changing the length of the line only on the wafer after coating. This ensures that the points after coating are never fitted to a larger range than the background points which would give a nonphysical result. Measurements by Romain Girard-Desprolet, [22].

It is clear from figure 10 that the 12th Order Method gives a much more stable result than the 1/R Method. For the StDev value in table 1 we have used the points between 20 and 28 mm. We see that the 12th Order Method gives a result that is more than 20 times better than the 1/R Method.

Table 1: Different lengths

	Method	StDev (10^{-6} m^{-1})	StDev^{-1} (km)
Different profile lengths	1/R	81.2	12.3
	12th	3.06	327.2

7.3.2 Perpendicular displacement

According to the theory, section 5.2, it should not matter where on the wafer one measures the curvature radius. As the wafer have the dimensions $50 \times 10 \times 1$ mm^3, we usually trace the surface profile in the middle of the wafer in the x_2 direction and parallel to the x_1 direction. In this test

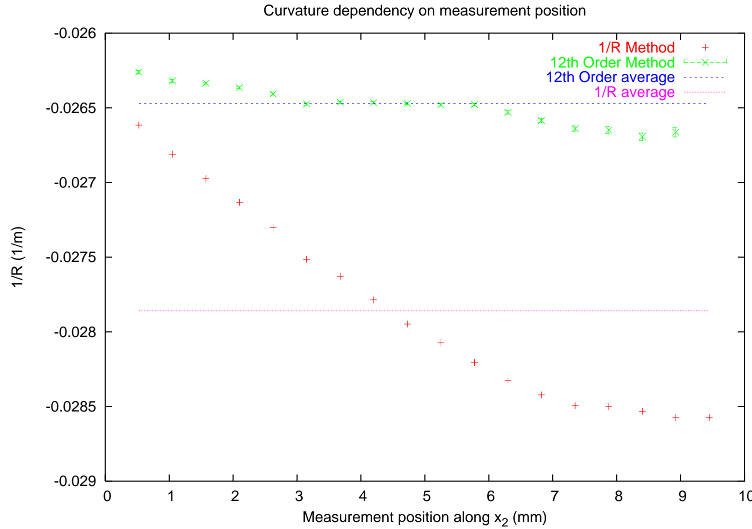

Figure 11: Here we have changed where on the wafer we have drawn the surface profile line. The red points are the inverse curvature radius calculated with the 1/R Method and the green points are the inverse curvature radius calculated with the 12th Order Method. Every surface profile were drawn parallel to the x_1 direction. On the x-axis it is indicated for which x_2-value the line was drawn. The wafer is 10 mm wide in total. Data from [22].

we have however changed the position along the x_2 direction of the surface profile line. The same x_2 position has been used on the wafer before and after coating. The results can be seen in figure 11. Measurements by Romain Girard-Desprolet, [22].

The results in figure 11 have a stable area towards the center of the wafer which is good since it is here, the surface profile is usually traced. It is also interesting that there are apparently no significant border effects even half a millimeter from the edge. There is however a systematic error, that is not totally eliminated with the 12th Order Method, since there is a tendancy for a higher curvature radius to the left on the wafer. From the results in table 2 we see a 40 times improvement from the 1/R Method to the 12th Order Method.

Table 2: Perpendicular displacement

	Method	StDev (10^{-6} m^{-1})	StDev^{-1} (km)
Perpendicular displacement	1/R	265	3.77
	12th	6.57	152.1

7.3.3 Changing the *FISBA* support

Romain Girard-Desprolet rebuilt the support for the interferometer to reduce vibrations. With the old support the interferometer hung in one aluminum arm, while he put an extra bar on the other side to make it rest on two feet, as seen in figure 7. He saw on the interference pattern that the apparatus was much more stable [22]. He took 10 measurements of the same sample with both the new and old support, but when he calculated the effective curvature radius, his StDev of the repeated measurements did not go down, as seen in table 3. We did not achieve a better precision with the 1/R Method neither, but with the 12th Order Method, the StDev is reduced by a factor 15 from the old to the new support and the improvement of the setup is now clearly seen. Measurements by Romain Girard-Desprolet, [22].

It should be noted that the 12th Order Method is not capable of designating a well-defined

curvature radius to a single wafer image neither. Only the difference between the before and after profiles makes sense. The radius differences used in the table, when there is only a before measurement, are thus calculated in another manner: At first a 12th order polynomial is fitted to one of the curvature profiles. Then the resulting function is subtracted from the data sets of the other measurements, and a second order polynomial is fitted to each resulting data set. This expresses how much the effective radius would differ between the different measurements if they where used together with an after image of the wafer to calculate the effective radius.

Table 3: Changing the *FISBA* support

	Method	StDev (10^{-6} m^{-1})	StDev^{-1} (km)
Old support	Romain	408	2.45
	1/R	538	1.86
	12th	476	2.10
New support	Romain	377	2.65
	1/R	763	1.31
	12th	29.4	34.1

7.3.4 Repeatability

Since the the time of Romain Girard-Desprolet, the interferometer support has been further improved with a better anti vibration table and the acoustic box, as seen in figure 7. To examine whether this has lowered the StDev, we have taken 10 pictures with the interferometer without touching anything. This is shown in table 4. The *short measurement time* correspond to a setting where 4 pictures are taken for each position of the interferometer and where the entire process will aswell be repeated 4 times. The *long measurement time* correspond to a setting where 16 pictures are taken for each position of the interferometer and where the entire process is repeated 16 times. This means that the long process is 16 times longer than the short, i.e. 4 minutes instead of 15 seconds per image.

When comparing the long and short measurement time StDev values in table 4, there is no significant difference. This means that we can just as well measure for 15 seconds as for 4 minutes, which makes the measurement process easier.

Table 4: Repeatability

	Method	StDev (10^{-6} m^{-1})	StDev^{-1} (km)
Short measurement time	1/R	9.34	107.1
	12th	1.57	637
Long measurement time	1/R	17.7	56.6
	12th	1.47	681.1

The 12th Order Method is still better than the 1/R Method, but now only by a factor 6 and 12, as shown in table 4. We also notice that the experimental setup has improved the precision by a factor 20 in comparison to Romain Girard-Desprolet's new support.

7.3.5 Moving the sample between measurements

To get a more realistic idea of the uncertainty we can expect from our real measurements, we took the sample out and put it back in, between each of these test measurements. *Deplaced with no readjustment* signifies that we have not readjusted the fringe pattern between each deplacement

and *deplaced with readjustment* signifies that we have readjusted the fringe pattern between each deplacement.

This is the uncertainty that should correspond most closely to the one in the real experiments. We see in table 5 a mere 5 times improvement over the 1/R Method, and the readjustment actually gives a worse result than the one with unchanged tilt settings.

Table 5: Readjustment between measurements

	Method	StDev (10^{-6} m^{-1})	StDev^{-1} (km)
Deplaced, no readjustment	1/R	55.4	18.1
	12th	7.95	125.8
Deplaced, w. readjustment	1/R	89.3	11.2
	12th	18.7	53.6

7.4 Conclusion on the choice of method

In sections 7.3.1 and 7.3.2 we have investigated the differences between the two methods when the curvature radius is measured in different manners on the same wafer image.

The effect of changing the length of the fit is examined in section 7.3.1. This is a test that focuses solely on the difference between the two methods without including measurement noise since it is the same wafer image that is used for all data points on figure 10. We see from table 1 that the 12th Order Method is 20 times better than the 1/R Method. This is an attempt to model the error arising from the problems of different measurement lengths, and we see that the 12th Order Method is superior in this case.

In section 7.3.2 it is examined how tracing the curvature profile at different x_2-values influences the measured radius. According to the Stoney equation (53) it should not matter where on the wafer the radius is measured. We see however in figure 11 a systematic trend towards a lower negative curvature radius for increasing x_2-values with both the 1/R Method and the 12th Order Method. The trend is much stronger for the 1/R method, and the 12th Order Method actually gives a close to constant curvature radius around the center of the wafer.

In sections 7.3.3, 7.3.4, and 7.3.5 the interferometer measurement precision has been tested. 7.3.3 is with Romain Girard-Desprolet's measurements while 7.3.4, and 7.3.5 are with our setup and measurements.

When examining the difference between Romain Girard-Desprolet's old and new support in section 7.3.3, the 1/R Method does not give a higher precision with the new support. With the 12th Order Method the precision is improved by a factor 15. This is an indication that the 1/R Method has a higher uncertainty than the physical instabilities.

If we compare the results from Romain Girard-Desprolet's new support in table 3 with our uncertainties in table 5 for the 12th Order Method, we see that the StDev is reduced by a factor 2. This improvement must be due to the anti vibration table and the acoustic box.

In section 7.3.4 we have taken multiple measurements without touching the setup. Here the 12th Order Method is 6 to 12 times better than the 1/R Method, but when readjusting the entire setup between each measurement in section 7.3.5, it is only 5 times better. This indicates that as the uncertainties from the measurement and the setup get bigger, the difference between the two methods decreases. Since the 12th Order Method is however still 5 times better than the 1/R Method, we have used it consistently for all our measurements in section 9.1.

From section 7.3.4 we get an idea of the precision of the interferometer when the sample lies in the exactly the same way for consecutive measurements. As seen in the third column of table 4, we are capable of distinguishing a perfect flat from a sphere with a radius of more than 600

kilometers which is more than one third of the radius of the moon. And this is on a wafer that is only 5 centimeters long!

To estimate the actual error we should implement, we have to look at the results from taking the wafer in and out of the sample holder and realigning it, section 7.3.5. This is the closest we get when testing to the measurement, alignment, and numerical errors of the real measurements. Since the highest StDev value in the table is $18.7 \cdot 10^{-6}\text{m}^{-1}$, we conclude that the uncertainty must be around $20 \cdot 10^{-6}\text{m}^{-1}$. This takes into account the fitting error, the taking in and out the wafer and readjusting the sample holder between each measurement.

7.5 Consequences of implenting the new method

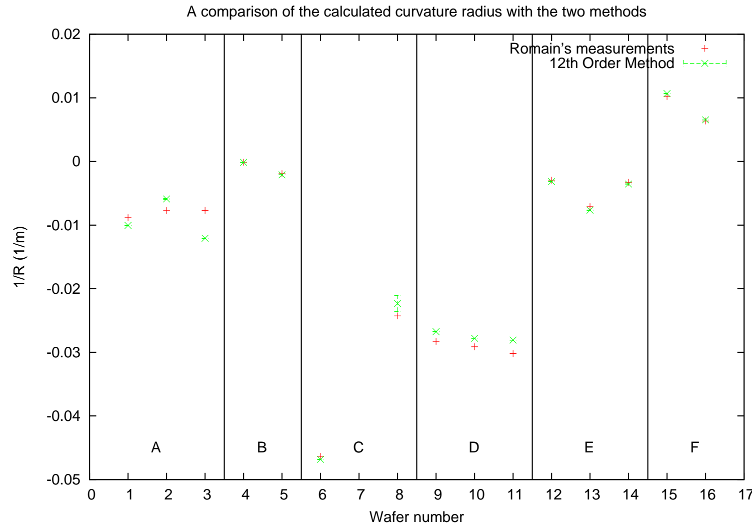

Figure 12: A comparison of Romain Girard-Desprolets calculated effective curvature radii and ours calculated with the 12th Order Method. The red points are the inverse curvature radius calculated by Romain Girard-Desprolet with the 1/R Method. The green points are our calculation of the inverse curvature raduis with the 12th Order Method. The error bars on the green points come from the fit. The points between each vertical line are for wafers with the same coating. For more details on each coating A-F see appendix D. Data from [22].

Romain Girard-Desprolet calculated the effective curvature radius of 15 wafers with different deposited films. As a final comparison between the two methods, we have recalculated these radii with the 12th Order Method. The result is seen in figure 12.

There is no overall shift in the values from the two methods, which is not suprising. The 12th order Method should only give an improve prrecision and not systematically differents values. All in all we do not seem to get a more consistent result for wafers with the same coating. The difference between the measured inverse curvature radius of the wafers with the same coating is much greater than the uncertainty due to the measurements, as seen in section 7.4, can explain. This means that there is a physical difference between two wafers with supposedly the same film.

The thickness of each layer is only estimated from the calibration of the sputtering process and not measured individually for each layer. It is therefore not possible to say if the difference in stress originates from a thickness difference due to the production process or if there is more complex reason for the different stresses in wafers with supposedly the same coating.

8 Evolution in stress over a period of 10 months

10 months have passed between Romain Girard-Desprolet's and our internships. Therefore we have had the possibility to investigate whether the stress has changed over time. The wafers have been stored in a closed box in an office building with normal temperature and moisture fluctuations.

For the stress values of the wafers from august 2010, we have used Romain Girard-Desprolet's interferometer images, but calculated the stress with the 12 Order Method. The new stress values from june 2011 were calculated from our own remeasurements of the wafers after coating and Romain Girard-Desprolet's measurements before coating with the 12 Order Method. The results can be seen in figure 13. All the green points lie quite close to the corresponding red points. The

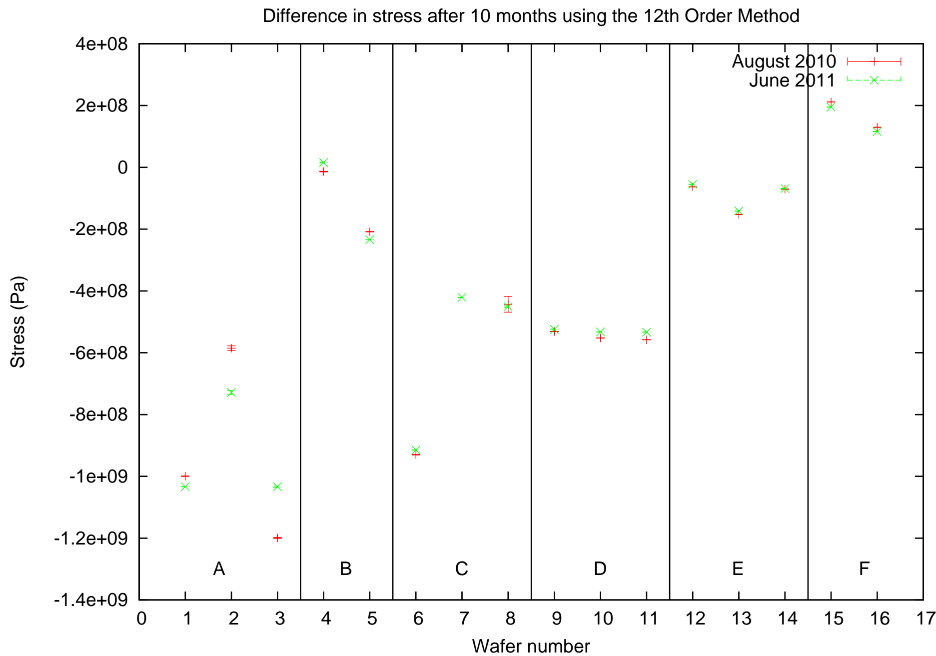

Figure 13: Here we see the evolution of the stress over 10 months. The red points are the stress calculated using the 12th Order Method with data from august 2010 by [22]. The green points are the stress calculated using the 12th Order Method with remeasurements of the wafers in june 2011. The error bars are estimated by *Gnuplot* from the fit. The points between each vertical line are for wafers with the same coating. For more details on each coating A-F, see appendix D.

only exception is wafers 1 to 5, for which the difference is up to 160 MPa. However, if one looks at the corresponding graph showing the curvature radii instead of the stress in appendix E, these points have the same difference. The five time bigger stress difference, is due to the fact that the coating is five time thinner, as seen in appendix D. Any difference in curvature will thus be multiplied by five for the stress. Since the errors are of the same size in curvature radius regardless of the stress, they cannot be due to a systematic change in the stress. This is further supported by the fact that there is no general tendency towards stress relaxation. This indicates that the supermirrors are stable and do not deform over time. It means that the stress is a static intrinsic property of the supermirrors after they have left the sputtering machine.

9 An empirical model for stress in supermirrors

The stress in a thin film depends on a lot of parameters: The deposition temperature, the pressure and type of gas used while sputtering, and of course the type of material deposited. For a multilayer structure one also has to consider the number of layers, their thickness and the proportion between the different materials. We have focused on multilayers made from titanium and a nickel alloy with 7% vanadium. The vanadium is added to ensure that the mirror will not polarize the neutron beam.

To narrow down the number of parameters, we decided to use an empirical model proposed by Christian Morawe [7] from the Multilayer Laboratory at *ESRF* [23]. It suggests that the stress is composed of three parts: One from the titanium, one from the nickel/vanadium, and one from the interfaces. In this way the force per length between the film and the substrate can be written

$$F = \sigma_{Ti} \cdot t_{Ti} + \sigma_{NiV} \cdot t_{NiV} + n \cdot (t_{Ti} + t_{NiV}), \quad (68)$$

where σ_{Ni} and σ_{TiV} are the stress in each material, which we search to determine, t_{Ti} and t_{NiV} are the total thickness of each material, n is the number of interfaces per thickness, and c is an empirical constant we want to determine. This can be rewritten to

$$\sigma = (\sigma_{Ti} - \sigma_{NiV})\Gamma + \sigma_{NiV} + c \cdot n, \quad (69)$$

with σ being the average stress in the multilayer, and Γ defined as

$$\Gamma = \frac{t_{Ti}}{t_{Ti} + t_{NiV}}. \quad (70)$$

We thus have the two variables Γ and n for determining σ_{NiV}, σ_{Ti}, and c.

9.1 Results

We have used periodic multilayers for determining the parameters and a supermirror to test whether the parameters we have found are consistent with measurements. In total we have made 7 different coatings: 6 periodic multilayers and one real supermirror. Three samples are coated for each type to get an idea of the precision of the sputtering, except for $n = 1/25$Å $\Gamma = 0.4$, for which we only have one wafer, and the supermirror deposition with two wafers.

The idea was to make two measurement series with periodic multilayers. One where the total thickness and the number of interfaces were kept constant, and hence only varying Γ. In the other the total thickness and Γ was kept constant and we were thus only varying the number of interfaces. A lack of time resulted in only a few data in the measurement series where the number of interfaces was varied. The calculated stess for each coating type can be seen in the table 6. Here the film stress σ_f is the mean value of the results from the three samples, and the

Table 6: The stress results from the periodic multilayers.

d_{Ti} (Å)	$d_{Ni/V}$ (Å)	layers	thickness (Å)	Γ	n ($^{-1}$)	samples	σ_f (MPa)	$\delta\sigma_f$ (MPa)
30	120	28	2100	0.2	1/75	3	-400	20
60	90	28	2100	0.4	1/75	3	-565	37
90	60	28	2100	0.6	1/75	3	-649	49
120	30	28	2100	0.8	1/75	3	-733	12
20	30	80	2000	0.4	1/25	1	-295	—
30	20	80	2000	0.6	1/25	3	-464	11

uncertainties of the measurements, $\delta\sigma_f$, are the standard deviation of the 3 results. The method

precision found in section 7 leads to an uncertainty in stress of about 3.7 MPa for our periodic multilayers. There is a much greater difference between wafers with the same coating than what the uncertainty on the measurements could have caused.

The layer thickness was estimated based on the calibration of the sputtering machine. Since it was not possible to actually measure the individual layer thicknesses, it is difficult to say if the stress difference comes from a thickness difference due to the production, or if there are more complex reasons for such a varying stress development.

The results are plotted in figure 14 which shows the film stress as a function of Γ for a fixed number of interfaces, and in figure 15 which shows the film stress as a function of the number of interfaces.

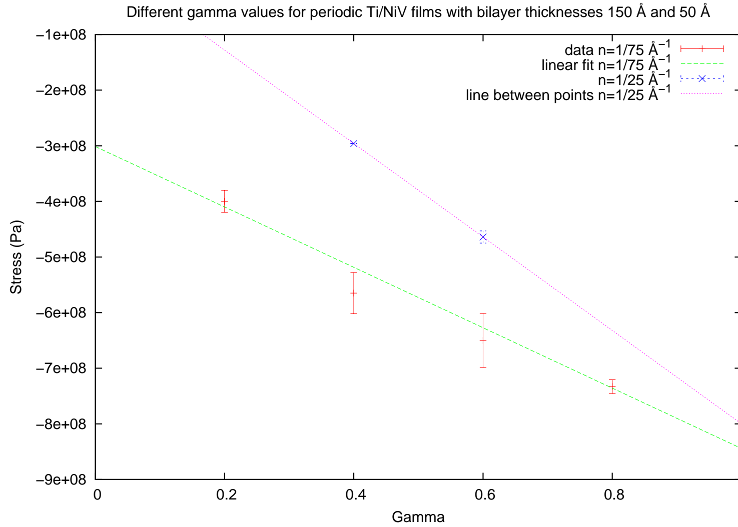

Figure 14: How the stress in a periodic multilayer depends on the proportion of titanium in the mirror. Γ is the titanium layer thickness divided by the total bilayer thickness. The points are the averages of the stress in the three wafers with the same coating, and the error bars are the StDev values of each set of three wafers. For the blue point at $\Gamma = 0.4$, we only had one wafer, so there is no errorbar. The red points are made with a bilayer thickness of 150 Å, and the blue points with a bilayer thickness of 50 Å. We have made a linear fit to the red points according to Morawe's model (69), with the points being weighted according to the uncertainty.

Since we only have four points with the same number of interfaces, it is neither possible to argue strongly for or against Morawe's model. The errorbars are big enough not to reject the model, but the points could easily have another behavior than linear. If we however assume that the linear model is correct, we get

$$\sigma_{NiV} - \sigma_{Ti} = -543 \pm 39 \text{ MPa} \tag{71}$$

$$\sigma_{Ti} + c \cdot 1/75\text{Å}^{-1} = -301 \pm 26 \text{ MPa.} \tag{72}$$

The uncertainties are given by *Gnuplot*, when it makes the linear fit taking the error bars on the points into account. We also see that the slopes for the $n = 1/25$ and the $n = 1/75$ data points are not that far from each other, which is what was predicted by Morawe's model.

To get values for all the parameters in the model, we have to study the dependency on the number of interfaces too. The results are shown in figure 15. When we only have two points for each Γ value, it is impossible to say anything about whether the stress depends linearly on n or not. We see however that the two lines have the same slope within the error bars, which is in good accordance with the model. If we take the average slope of these two graphs, we get an

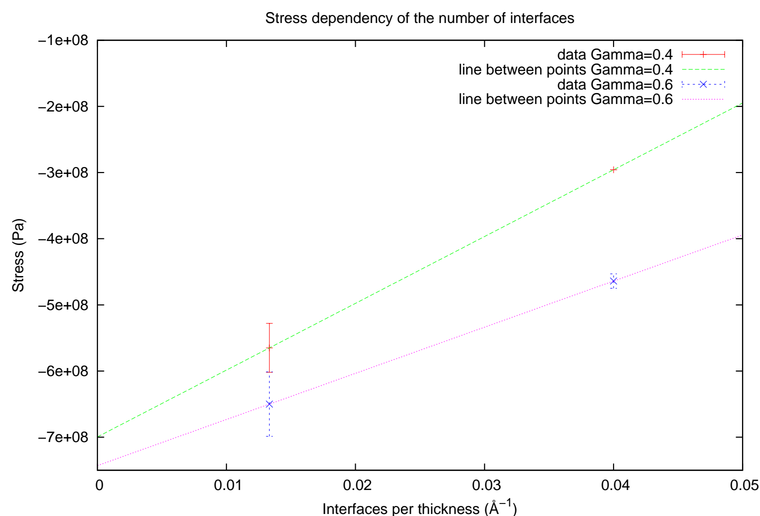

Figure 15: The dependency of the stress on the number of interfaces in a periodic titanium nickel/vanadium multilayer. On the x-axis we have the number of interfaces per thickness, which is the reciprocal of the average single layer thickness. The error bars are the StDev values of the three wafers with the same deposition, and the points are the averages of the stress in the three wafers. The lines are used to calculate c from (69).

estimate of the value of c. This gives

$$c = 8.53 \pm 2.21 \text{ GPa}\cdot\text{Å}, \tag{73}$$

with the uncertainty being the StDev of the two slopes.

Of course we can not have much confidence in the values now determined because of the lack of points on the graphs 14 and 15. They can however serve in the following example of how the parameters should be determined and tested.

We want to test the found parameter values on a real supermirror. At first we need to isolate the parameters σ_{NiV} and σ_{Ti}. This gives

$$\sigma_{Ti} = -415 \pm 39 \text{ MPa} \tag{74}$$

$$\sigma_{NiV} = -958 \pm 55 \text{ MPa}. \tag{75}$$

The supermirror described in appendix F had on average for all the layers

$$\Gamma = 0.29 \tag{76}$$

$$n = 1/229\text{Å}. \tag{77}$$

When we insert the values for Γ and n in Morawe's model (69) with the parameters (73), (74), and (75), we predict

$$\sigma_{prd} = -535 \pm 33 \text{ MPa}. \tag{78}$$

The measured stress was

$$\sigma_{msr} = -579 \pm 7 \text{ MPa}. \tag{79}$$

9.2 Changing the sputtering atmosphere

It has been found empirically [24–26] that adding air to the argon used for sputtering increases the reflectivity of the supermirrors. Our wafers have been sputtered using only argon for the titanium layers, and 80% argon and 20 % air for the nickel/vanadium layers, which is standard in the supermirror production at *ILL*.

We have examined whether the addition of air changes the stress. For this we have made a periodic titanium nickel/vanadium multilayer with $n = 1/75\text{Å}$ and $\Gamma = 0.4$ using only argon as sputtering atmosphere. The results from this multilayer and a multilayer that is identical except for the addition of air can be found in table 7. We have made three wafers for each, and the

Table 7: The difference in stress due to addition of air in the sputtering process.

	d_{Ti} (Å)	$d_{Ni/V}$ (Å)	layers	thickness (Å)	samples	σ_f (MPa)	$\delta\sigma_f$
with air	60	90	28	2100	3	-565	37
no air	60	90	28	2100	3	-680	6

uncertainty is the StDev value of the three. $\delta\sigma_f$ is 6 times bigger with air than without, but we have not made enough samples to draw any conclusion. As there is a significantly increased stress in the films when sputtered without air, the addition of air in the production is further supported.

10 Discussion

The parameter values from section 9.1 can, with our limited measurements, not be considered well determined. Nevertheless, the predicted value for the stress in the supermirror differ by only 8% which is consistent with the errorbars. This is certainly promising for further investigations. First of all more periodic multilayers should be examined so the dependency on Γ and n can be clarified. Then the stress in different supermirrors should be measured so the model's ability to predict stress can be evaluated.

When looking at previous studies of the subject, both [27], [28] and [7] have a found a linear dependency in Γ when working with $Fe_{89}Co_{11} - Si$, $Mo - Si$ and $Ru - B_4C$ multilayers. Even though they are not working with the same materials as us, we expect the general behavior to be the same. The stress due to interfaces is in general more complicated since interdiffusion of atoms between the layers, interface roughness, and the contribution from the interface between the substrate and the film need to be taken into consideration. A combination of curvature measurements and x-ray diffraction, as in [29–31], would be an interesting next step in the process.

11 Conclusion

Our goal was to find a model and determine the parameters for stress in supermirrors.

We started by evaluating the existing method for measuring stress in thin films, the 1/R method, and found compelling reasons for a change of method. This resulted in the development of the 12th Order Method described in section 7.2. This method is much more stable and precise than the old 1/R Method. When all uncertainties are taken into account, the error on the reciprocal curvature radius is below $20 \cdot 10^{-6}\text{m}^{-1}$, which is 5 times better than with the old 1/R Method.

We have started the process of parameter determination using the model of Morawe (69), and the first results look promising: For the supermirror described in appendix F, an experimental stress value of -579 ± 7 MPa have been found, compared to -535 ± 33 MPa when using the

model with the parameters determined in section 9.1. We thus see a difference of only 8%, which is explainable by the error bars. This is encouraging for further investigations.

Hopefully such a model can one day be taken into account in supermirror production and facilitate the development of supermirrors with a higher m-value.

References

[1] ILL Institut Laue-Langevin. http://www.ill.eu/. 2011.

[2] ESS The European Spallation Source. http://ess-scandinavia.eu/. 2011.

[3] Mirror and Metrology Laboratory at ESRF. http://www.esrf.eu/instrumentation/xray-optics/mirror-and-metrology-lab. 2011.

[4] ESRF European Synchrotron Radiation Facility. http://www.esrf.eu/. 2011.

[5] M. Senthil Kumar, P. Böni, S. Tixier, and D. Clemens. Stress minimisation in sputtered ni/ti supermirrors. *Physica B*, 241-243:95–97, 1998.

[6] G. G. Stoney. The tension of metallic films deposited by electrolysis. *R. Soc. London*, 82:172–175, 1909.

[7] Ch. Morawe, J-Ch. Peffen, and K. Friedrich. In-situ stress measurements of sputtered multilayers. Proceedings Paper, Advances in X-Ray/EUV Optics and Components V, 2010.

[8] Masahiko Utsoro and Vladimir K. Ignatovich. *Handbook of neutron optics*. Wiley-VCH, Weinheim, 2010.

[9] P. Böni. Supermirror-based beam devices. *Physica B*, 234-236:1038–1043, 1997.

[10] F. Mezei. Novel polarized neutron devices: supermirror and spin component amplifier. *Communications on physics*, 1:81–85, 1976.

[11] John B. Hayter and H. A. Mook. Discrete thin-film multilayer design for x-ray and neutron supermirrors. *J. Appl. Cryst.*, 22:35–41, 1989.

[12] G. L. Squires. *Thermal Neutron Scattering*. Cambridge University Press, Cambridge, 1978.

[13] Varley F. Sears. *Neutron optics*. Oxford University Press, 200 Madison Avenue, New York, 1989.

[14] John Lekner. *Theory of reflection*. Martinus Nijhoff publishers, Dordrecht, 1987.

[15] Kasturi L. Chopra. *Thin film phenomena*. McGraw-Hill Book Company, New York, 1969.

[16] Richard P. Feynman, Robert B. Leighton, and Matthew Sands. *The Feynman lectures on physics volume 2*. Addison-Wesley, 1964.

[17] G. C. A. M. Janssen, M. M. Abdalla, F. van Keulen, B. R. Pujada, and B. van Venrooy. Celebrating the 100th anniversary of the stoney equation for film stress: Developments from polycrystalline steel strips to single crystal silicon wafers. *Thin solid films*, 517:1858–1867, 2009.

[18] L. D. Landau and E. M. Lifschitz. *Lehrbuch der theoretischen physik band 7, elastizitätstheorie*. Akademie-verlag, Berlin, 1966.

[19] Brian D. Harper and Chih-Ping Wu. A geometrically nonlinear model for predicting the intrinsic film stress by the bending-plate method. *International journal of solids and structures*, 26 (5-6):511–525, 1990.

[20] P.J. Kelly and R.D. Arnell. Magnetron sputtering: a review of recent developments and applications. *Vacuum*, 56:159–176, 2000.

[21] FISBA Optik μShape. http://www.fisba.ch/english/company/default.cfm. 2011.

[22] Romain Girard-Desprolet. Etude des contraintes dans les optiques multicouches pour les neutrons. Unpublished, ILL, August 2010.

[23] The Multilayer Laboratory at ESRF. http://www.esrf.eu/instrumentation/xray-optics/multilayer-lab. 2011.

[24] M. Senthil Kumar, P. Böni, and M. Horisberger. Relationship between neutron reflectivity, electrical resistance, stress and embrittlement in reactively sputtered ni/ti multilayers and supermirrors. *Physica B*, 385-386:1265–1267, 2006.

[25] M. Senthil Kumar, P. Böni, and D. Clemens. Mechanical and structural properties of ni/ti multilayers and films - an application to neutron supermirrors. *Journal of applied physics*, 84:6940–6942, 1998.

[26] M. Senthil Kumar, P. Böni, and D. Clemens. Stress minimisation in sputtered ni/ti supermirrors. *Physica B*, 241-273:95–97, 1998.

[27] Anke Teichert, Thomas Krist, and Ferenc Mezei. Stress dependence in fe89co11–si multilayers on layer thicknesses. *Physica B*, 385–386:1262–1264, 2006.

[28] S.S. Andreev, N.N. Salashchenko, L.A. Suslov, and A.N. Yablonsky S.Yu. Zuev. Stress reduction of mo/si multilayer structures. *Nuclear Instruments and Methods in Physics Research A*, 470:162–167, 2001.

[29] K. O. Schweitz, J. Bœttiger, J. Chevallier, R. Feidenhans'l, M. M. Nielsen, and F. B. Rasmussen. Interface stress in au-ni multilayers. *Journal of applied physics*, 88:1401–1406, 2000.

[30] D. Josell, J.E. Bonevich, I. Shao, and R.C. Cammarata. Measuring the interface stress: Silver/nickel interfaces. *Journal of materials research*, 14:4358–4365, 1999.

[31] F. Spaepen. Interfaces and stresses in thin films. *Acta Materialia*, 48:31–42, 2000.

A *Gnuplot* script for calculating the curvature radius

```
# This script can be used to determine b2 (and thus the effective curvature radius)
for each sample when having a profile of the wafer before deposition and one
after. The profile data file of the wafer before sputtering is called
"xx-before" and for the wafer after sputtering "xx-after".

##################################
# - This is just the preamble.

reset
set output "xx.eps"
set term postscript eps color

##################################
# - f(x) is the 12th order polynomial that is fitted to the before data.

f(x)= a0 + a1*x + a2*x**2 + a3*x**3 + a4*x**4 + a5*x**5 + a6*x**6 + a7*x**7 +
a8*x**8 + a9*x**9 + a10*x**10 + a11*x**11 + a12*x**12

#An example of parameter values:

a0              = 1265.79
a1              = 20.6932
a2              = -5.92349
a3              = 0.0668554
a4              = -0.00524379
a5              = -0.000613474
a6              = 2.33256e-05
a7              = 9.31314e-07
a8              = -3.92301e-08
a9              = -4.75072e-10
a10             = 2.49512e-11
a11             = 3.15014e-18
a12             = 9.63838e-20

# now we fit f(x) to the before data. The <via> command tells the program which
parameters from f(x) should be used for fitting:

fit f(x) "xx_before"  via a0, a1, a2, a3, a4, a5, a6, a7, a8, a9, a10, a11, a12

# Here comes the fit to the new data:
g(x)= f(x-x0)+ h(x)

#Parameter examples:

x0              = -0.00745445
b0              = -34.2405
b1              = -0.436914
```

```
b2              = -23.578

fit g(x) "xx_after" via x0, b0, b1, b2

# And finally the plot.

plot "xx_before" u 1:2 title "xx-before", "xx_after" u 1:2 title "xx_after",
f(x) title "fit before", g(x) title "fit after"
reset

# The effective curvature in units of 1/m is b2/500.
```

B Difference between the 1/R Method and the 12th Order Method

In this section we will thoroughly explain the difference between the two methods for calculating the effective curvature radius.

B.1 How the fit works

Our fits are done by the least squares method. This works in the following way:

Let there be given a data set of measurements (x_i, y_i) where x_i could be position along the wafer and y_i the measured height. We define a function used for the fit, $f(x)$, which contains the fit parameters $\vec{b}$. All errors on y_i are assumed to be identical. The values of $\vec{b}$ are found by minimizing the function

$$\chi^2 = (f(x_1) - y_1)^2 + (f(x_2) - y_2)^2 + ... + (f(x_n) - y_n)^2. \tag{80}$$

It is minimized by solving the equations for the derivatives

$$\frac{\partial \chi^2}{\partial b_i} = 0. \tag{81}$$

If $f(x)$ is a linear function of $\vec{b}$, it can be written

$$f(x) = b_0 h_0(x) + b_1 h_1(x) + b_2 h_2(x) + ... + b_m h_m(x), \tag{82}$$

and the minimisation gives

$$\sum_{i=1}^{n} (f(x_i) - y_i) h_0(x_i) = 0 \tag{83}$$

$$\sum_{i=1}^{n} (f(x_i) - y_i) h_1(x_i) = 0 \tag{84}$$

$$\sum_{i=1}^{n} (f(x_i) - y_i) h_2(x_i) = 0 \tag{85}$$

$$. \tag{86}$$

$$. \tag{87}$$

$$. \tag{88}$$

$$\sum_{i=1}^{n} (f(x_i) - y_i) h_m(x_i) = 0. \tag{89}$$

B.2 Substrate curvature

In our case, we want to calculate how much the deposition of a film bends a silicon wafer. We therefore compare the surface of the wafer before deposition, described by

$$\mathbf{B} = \begin{pmatrix} x_1 & y_1 \\ x_2 & y_2 \\ . & . \\ . & . \\ . & . \\ x_n & y_n \end{pmatrix}, \tag{90}$$

with the surface after, described by

$$\mathbf{A} = \begin{pmatrix} x_1 & y_1 + z_1 \\ x_2 & y_2 + z_2 \\ . & . \\ . & . \\ . & . \\ x_n & y_n + z_n \end{pmatrix}. \tag{91}$$

The effective curvature radius is defined as c_2 when

$$j(x) = c_0 + c_1 x + c_2 x^2 \tag{92}$$

is fitted to

$$\mathbf{C} = \begin{pmatrix} x_1 & z_1 \\ x_2 & z_2 \\ . & . \\ . & . \\ . & . \\ x_n & z_n \end{pmatrix}. \tag{93}$$

B.3 The 1/R Method

With the 1/R Method one fits

$$f(x) = b_0 + b_1 x + b_2 x^2 \tag{94}$$

to **B**, and

$$g(x) = a_0 + a_1 x + a_2 x^2 \tag{95}$$

to **A**. Fitting gives:

$$\sum_{i=1}^{n} (b_0 + b_1 x_i + b_2 x_i^2 - y_i) x_i^2 = 0 \quad \text{and} \tag{96}$$

$$\sum_{i=1}^{n} (a_0 + a_1 x_i + a_2 x_i^2 - y_i - z_i) x_i^2 = 0 \Rightarrow \tag{97}$$

$$\sum_{i=1}^{n} (a_0 - b_0 + (a_1 - b_1) x_i + (a_2 - b_2) x_i^2 - z_i) x_i^2 = 0. \tag{98}$$

The effective curvature is then

$$c_2 = a_2 - b_2. \tag{99}$$

We will show that this is equivalent to fitting

$$i(x) = d_0 + d_1 x + d_2 x^2 + f(x) \tag{100}$$

to **A** via d_0, d_1, d_2, after having determined b_0, b_1, b_2 from **B**. This results in

$$\sum_{i=1}^{n} (b_0 + b_1 x_i + b_2 x_i^2 - y_i) x_i^2 = 0 \quad \text{and} \tag{101}$$

$$\sum_{i=1}^{n} ((b_0 + d_0) + (b_1 + d_1) x_i + (b_2 + d_2) x_i^2 - y_i - z_i) x_i^2 = 0 \Rightarrow \tag{102}$$

$$\sum_{i=1}^{n} (d_0 + d_1 x_i + d_2 x_i^2 - z_i) x_i^2 = 0. \tag{103}$$

Thus

$$d_j = a_j - b_j \tag{104}$$

since there is only one solution to the set of equations (84)-(**??**), and especially

$$d_2 = c_2. \tag{105}$$

B.4 The 12th Order Method

In the 12th Order Method, we use

$$f(x) = b_0 + b_1 x + b_2 x^2 + ... + b_{12} x^{12} \tag{106}$$

to get a better fit to **B**. Then

$$i(x) = d_0 + d_1 x + d_2 x^2 + f(x) \tag{107}$$

is fitted to **A**. This results once again in a series of equations, whereas the two we are interested in have the form

$$\sum_{i=1}^{n} (f(x_i) - y_i) x_i^2 = 0 \quad \text{and} \tag{108}$$

$$\sum_{i=1}^{n} (f(x_i) + d_0 + d_1 x_i + d_2 x_i^2 - y_i - z_i) x_i^2 = 0 \Rightarrow \tag{109}$$

$$\sum_{i=1}^{n} (d_0 + d_1 x_i + d_2 x_i^2 - z_i) x_i^2 = 0, \tag{110}$$

which is identical to (103). We thus see that it gives exactly the same curvature as with the old method. Why then bother with polynomials of the 12th order? That becomes clear when we take into account that it is not possible to measure the after profile on exactly the same interval as the one from before film deposition. In other words, **A** is redefined to

$$\mathbf{A} = \begin{pmatrix} x_{1+q} + \Delta & y_{1+q} + z_{1+q} \\ x_{2+q} + \Delta & y_{2+q} + z_{2+q} \\ . & . \\ . & . \\ . & . \\ x_{n-p} + \Delta & y_{n-p} + z_{n-p} \end{pmatrix}. \tag{111}$$

Our usual equations then become

$$\sum_{i=1}^{n} (f(x_i) - y_i) x_i^2 = 0 \quad \text{and} \tag{112}$$

$$\sum_{i=1+q}^{n-p} (f(x_i + \Delta) + d_0 + d_1(x_i + \Delta) + d_2(x_i + \Delta)^2 - y_i - z_i)(x_i + \Delta)^2 = 0, \tag{113}$$

so we can not just subtract them as above. For this to give $d_2 = c_2$, there are two conditions: $f(x)$ must fit really well to **B**, and **C** must have the shape of a parabola. The first condition is easily met, since **B** traces a slowly varying continuous function. Therefore it is just a question of choosing a polynomial of sufficiently high order for fitting. A 12th order polynomial has prooven

to suffice in our case, se appendix C. The second condition is also met since the stoney equation (66) predicts a spherical curvature. This is in our case practically the same as a parabola, since the curvature radius is big compared to the wafer length.

Because of the Δ term in (113), we introduce an extra fit parameter x_0, so equation (113) is substituted by

$$\sum_{i=1+q}^{n-p} (f(x_i + \Delta + x_0) + d_0 + d_1(x_i + \Delta) + d_2(x_i + \Delta)^2 - y_i - z_i)(x_i + \Delta)^2 = 0. \tag{114}$$

This takes into account the shift in traced curvature profile on the wafer after deposition compared to the wafer before deposition. Since the fit for $f(x)$ to **B** is good, each term in the sum (112) will be small. Therefore

$$f(x_i) - y_i \ll z_i, \tag{115}$$

and equation (114) gives nearly the same values for d as

$$\sum_{i=1+q}^{n-p} (d_0 + d_1(x_i + \Delta) + d_2(x_i + \Delta)^2 - z_i)(x_i + \Delta)^2 = 0. \tag{116}$$

Since **C** is close to a parabola, the fit (116) gives the same value for d_2 independently of Δ. We thus see that $d_2 = c_2$ independently of Δ, p, and q.

To summarize: If the initial fit function fits well to the initial profile, and if the final fit function fits well to the final profile, the interval of fitting and shift on the x-axis does not matter. On the other hand, if one fits on the exact same interval before and after, the quality of the fit does not matter, as shown in equation (103). We are however working with different fitting intervals and an initial wafer curvature that is more complicated than a parabola, so we have to use the 12th Order Method.

C The polynomial order

In the method development process we have examined the dependency on the polynomial order when calculating the curvature radius and the displacement of the profiles before and after coating. Figure 16 shows the curvature radius as a function of the polynomial order, and figure 17 shows the displacement as a function of the polynomial order. A polynomial of the 12th order seems to ensure that the curvature radius and displacement is well-defined.

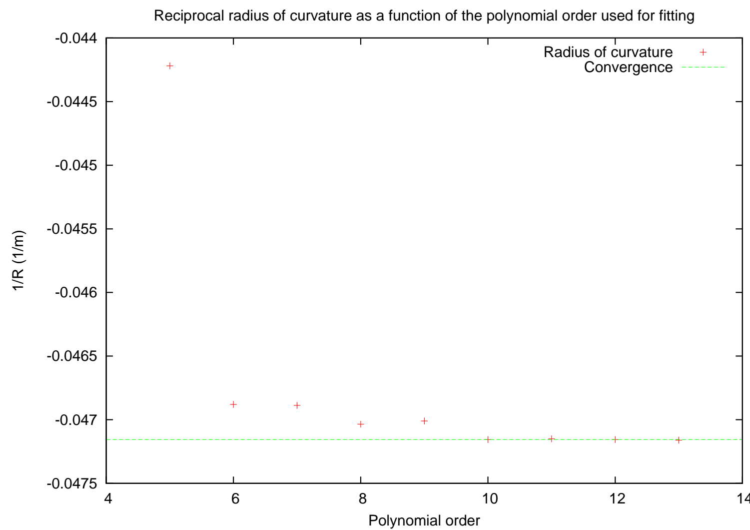

Figure 16: The plot shows the curvature radius as a function of the polynomial order used when fitting to the profile before coating. The convergence line is calculated from the values between order 10 and 13.

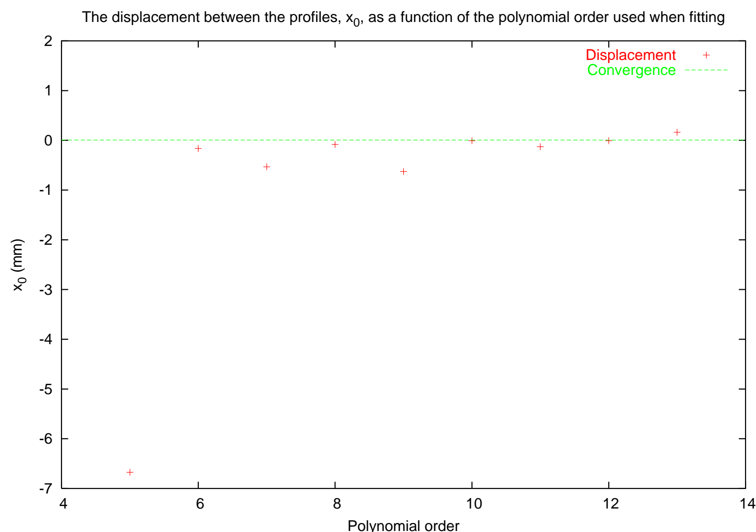

Figure 17: The plot shows the displacement as a function of polynomial order used when fitting to the profile before coating. The convergence line is calculated from the values between order 10 and 13.

D The coating on Romain Girard-Desprolet's samples.

An overview of the coating of each sample.

Table 8: Periodic multilayer coating, [22].

	Sample number	Layers	d_{Fe} (Å)	d_{Si} (Å)
A	1	1	—	1000
	2	1	—	1000
	3	1	—	1000
B	4	1	1000	—
	5	1	1000	—
C	6	10	50	950
	7	10	50	950
	8	10	50	950
D	9	10	300	700
	10	10	300	700
	11	10	300	700
E	12	10	700	300
	13	10	700	300
	14	10	700	300
F	15	10	950	50
	16	10	950	50

E Evolution in curvature over a period of 10 months

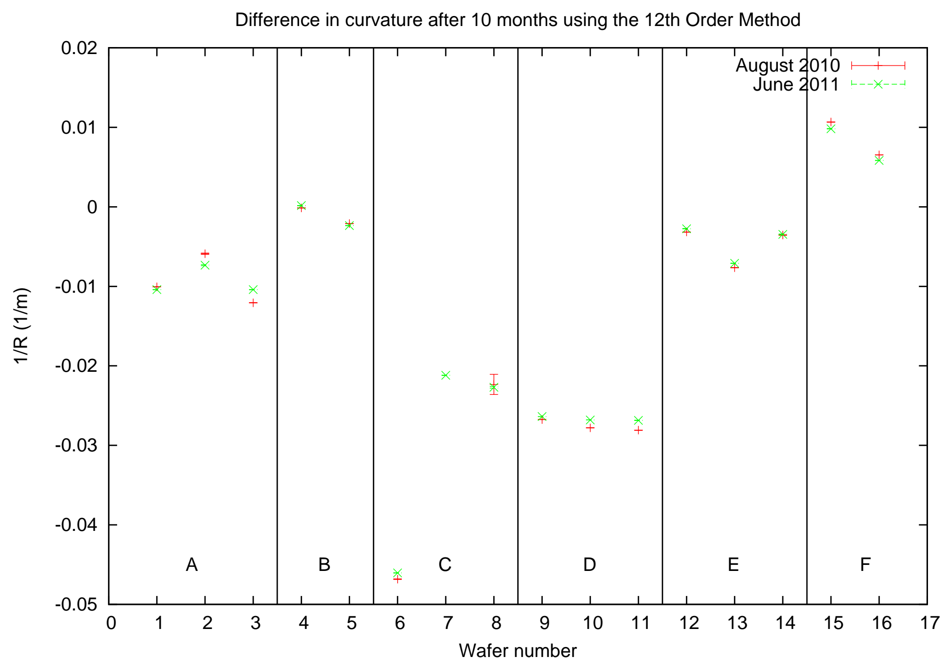

Figure 18: Here we see the evolution of the effective radius of curvature over 10 months. The red points are the radii calculated using the 12th Order Method with data from august 2010 by [22]. The green points are the radii calculated using the 12th Order Method with remeasurements of the wafers in june 2011. The error bars are estimated by *Gnuplot* from the fit. The points between each vertical line are for wafers with the same coating. For more details on each coating A-F, see appendix D.

F The Ti - NiV supermirror

The Titanium - NickelVanadium supermirror was composed of 16 layers in total, i.e. 8 bilayers.

Bilayer number	Ti (Å)	NiV (Å)
1	107	184,6
2	111	200
3	115,2	218,2
4	119,7	240
5	124,6	266,7
6	130	300
7	154,4	401,2
8	200	799,9
Sum	1061,9	2610,6

Total thickness	3672,5 Å
n	1/229 $Å^{-1}$
Gamma	0.289